

Deformation-Recovery Diffusion Model (DRDM): Instance Deformation for Image Manipulation and Synthesis

Jian-Qing Zheng^{a,b,**}, Yuanhan Mo^{c,*}, Yang Sun^c, Jiahua Li^c, Fuping Wu^c, Ziyang Wang^d, Tonia Vincent^a, Bartłomiej W. Papież^c

^aThe Kennedy Institute of Rheumatology, University of Oxford, U.K.

^bChinese Academy of Medical Sciences Oxford Institute, University of Oxford, U.K.

^cBig Data Institute, University of Oxford, U.K.

^dDepartment of Computer Science, University of Oxford, Oxford, U.K.

Project page: https://jianqingzheng.github.io/def_diff_rec/

Abstract

In medical imaging, the diffusion models have shown great potential in synthetic image generation tasks. However, these models often struggle with the interpretable connections between the generated and existing images and could create illusions. To address these challenges, our research proposes a novel diffusion-based generative model based on deformation diffusion and recovery. This model, named Deformation-Recovery Diffusion Model (DRDM), diverges from traditional score/intensity and latent feature-based approaches, emphasizing morphological changes through deformation fields rather than direct image synthesis. This is achieved by introducing a topological-preserving deformation field generation method, which randomly samples and integrates a set of multi-scale Deformation Velocity Fields (DVF). DRDM is trained to learn to recover unreasonable deformation components, thereby restoring each randomly deformed image to a realistic distribution. These innovations facilitate the generation of diverse and anatomically plausible deformations, enhancing data augmentation and synthesis for further analysis in downstream tasks, such as few-shot learning and image registration. Experimental results in cardiac MRI and pulmonary CT show DRDM is capable of creating diverse, large (over 10% image size deformation scale), and high-quality (negative rate of the Jacobian matrix's determinant is lower than 1%) deformation fields. The further experimental results in downstream tasks, 2D image segmentation and 3D image registration, indicate significant improvements resulting from DRDM, showcasing the potential of our model to advance image manipulation and synthesis in medical imaging and beyond.

Keywords: Image Synthesis, Generative Model, Data Augmentation, Segmentation, Registration

1. Introduction

Image synthesis, a captivating domain within artificial intelligence, has been revolutionized by the advent of deep learning technologies (Zhan et al., 2023). It in-

volves generating new images from existing ones or from scratch, guided by specific patterns, features, or constraints. Deep learning, with its ability to learn hierarchical representations, has become the cornerstone of advancements in image synthesis, enabling applications that range from artistic image generation to the creation of realistic training data for machine learning models.

The heart of image synthesis via deep learning lies in the neural networks' capability to understand and manipulate complex data distributions. Generative models,

*These authors contributed equally to this work

**Corresponding author

Email address: jianqing.zheng@ndm.ox.ac.uk, outlook.com} (Jian-Qing Zheng)

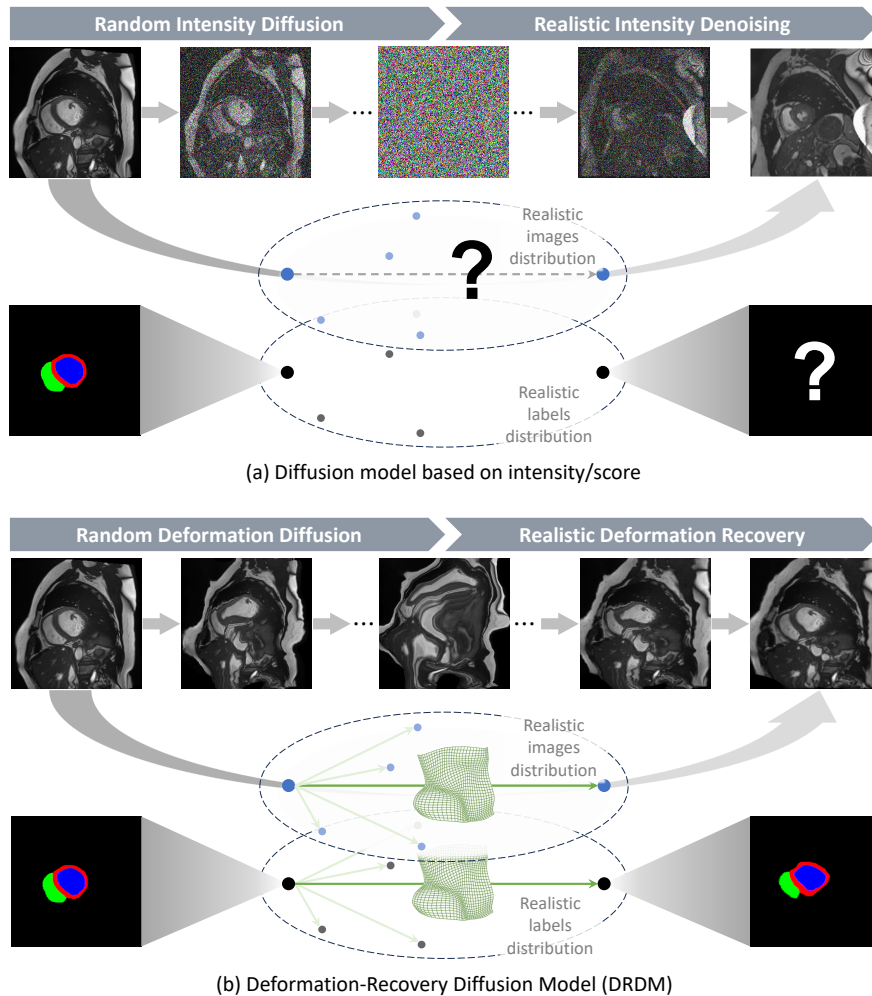


Figure 1: (a) Diffusion model based on intensity/score can synthesize realistic images, but without a known relationship with other existing real subjects, and thus unknown labels; (b) DRDM deforms realistic images with generated deformation, representing the anatomical changes, which can also be applied to pixel-wise labels, thus benefiting downstream tasks.

particularly Variational Autoencoders (VAEs) (Kingma and Welling, 2013) and Generative Adversarial Networks (GANs) (Goodfellow et al., 2020), have emerged as powerful tools for this purpose. VAEs focus on learning a latent space representation, enabling the generation of new images by sampling from this space. GANs, on the other hand, consist of a generator that synthesizes images and a discriminator that judges their authenticity. The training process continues until the system reaches a Nash equilib-

rium, where the generator produces realistic images that the discriminator can no longer easily distinguish from real ones (Goodfellow et al., 2020).

Recently, intensity/score-based diffusion models, specifically Denoising Diffusion Probabilistic Model (DDPM)s (Ho et al., 2020), have shown excellent performance in generative modeling across various computer vision domains. These models generate high-fidelity data and exhibit properties such as scalability and

trainability. Furthermore, feature-based latent diffusion models (Rombach et al., 2022) enable the integration of multimodal data, such as text, into the diffusion process.

In medical imaging, diffusion models have been utilized for tasks, such as synthetic medical image generation (Pinaya et al., 2022; Ju and Zhou, 2024; Du et al., 2023), biomarker quantification (Gong et al., 2023), anomaly detection Li et al. (2023); Bercea et al. (2023); Liang et al. (2023), image segmentation (Graf et al., 2023) and image registration (Qin and Li, 2023; Gao et al., 2023). These methods are capable of generating highly lifelike images but still suffer from potential issues such as producing visually plausible yet unrealistic artifacts and the inability of generated images to establish meaningful and interpretable relationships with pre-existing images, as illustrated in Figure 1(a). This limitation hinders their applicability in tasks, such as image segmentation, that require precise understanding and correlation with real data (Kazerouni et al., 2023).

Generating deformation fields rather than images through diffusion models can address this issue by focusing on anatomical changes. Several previous works (Kim et al., 2022; Kim and Ye, 2022; Starck et al., 2024) have attempted to generate deformation fields using an image registration framework combined with diffusion models. However, they still employ diffusion-denoising approaches based on intensities (Kim et al., 2022; Kim and Ye, 2022) or hidden-feature (Starck et al., 2024), depending on registration frameworks to guide and constrain the rationality of the generated deformations. Consequently, the deformations generated by these methods are typically limited to the interpolation of deformation processes between pairs of images (Kim et al., 2022; Kim and Ye, 2022) or the deformation of atlas images (Starck et al., 2024), which does not allow for the generation of more diverse deformations for each individual image.

The noise added on intensity introduced in the existing diffusion models (Sohl-Dickstein et al., 2015; Ho et al., 2020; Song et al., 2020) is fully independent of each other pixel/voxel and yields a normal distribution. However, our target is to deform an image rather than generate a new one, and the deformation vector at each organ is typically not independent. Therefore, we need to investigate the modeling of deformation and develop a diffusion technique based on the realistic distribution of deformation.

In our paper, we propose a novel diffusion genera-

tive model based on deformation diffusion-and-recovery, which is a deformation-centric version of the noising and denoising process. Named Deformation-Recovery Diffusion model (DRDM), this model aims to achieve realistic and diverse anatomical changes as shown in Figure 1(b). As illustrated in Figure 2, the framework includes random deformation diffusion followed by realistic deformation recovery, enabling the generation of diverse deformations for individual images. Our main contributions are as follows.

- **Instance-specific deformation synthesis:** To the best of our knowledge, this is the first study to explore diverse deformation generation for one specific image without any atlas or another reference image required;
- **Deformation Diffusion model:** We propose a novel diffusion model method based on deformation diffusion and recovery, rather than intensity/score diffusion (Kim et al., 2022; Kim and Ye, 2022) or latent feature diffusion (Starck et al., 2024) based on registration framework;
- **Multi-scale random deformation velocity field sampling and integrating:** The method of multi-scale random Dense Velocity Field (DVF) sampling and integrating is proposed to create deformation fields with physically possible distributions randomly for DRDM training;
- **Training from scratch without annotation:** The training of DRDM does not require any annotation by humans or an external (registration or optical/scene flow) model/framework;
- **Data augmentation for few-shot learning:** The diverse deformation field generated by DRDM is used on both image and pixel-level segmentation, to augment morphological information without changes in anatomical topology. Thus it enables augmented data for few-shot learning tasks;
- **Synthetic training for image registration:** The synthetic deformation created by DRDM can be used to train an image registration model without any external annotation;

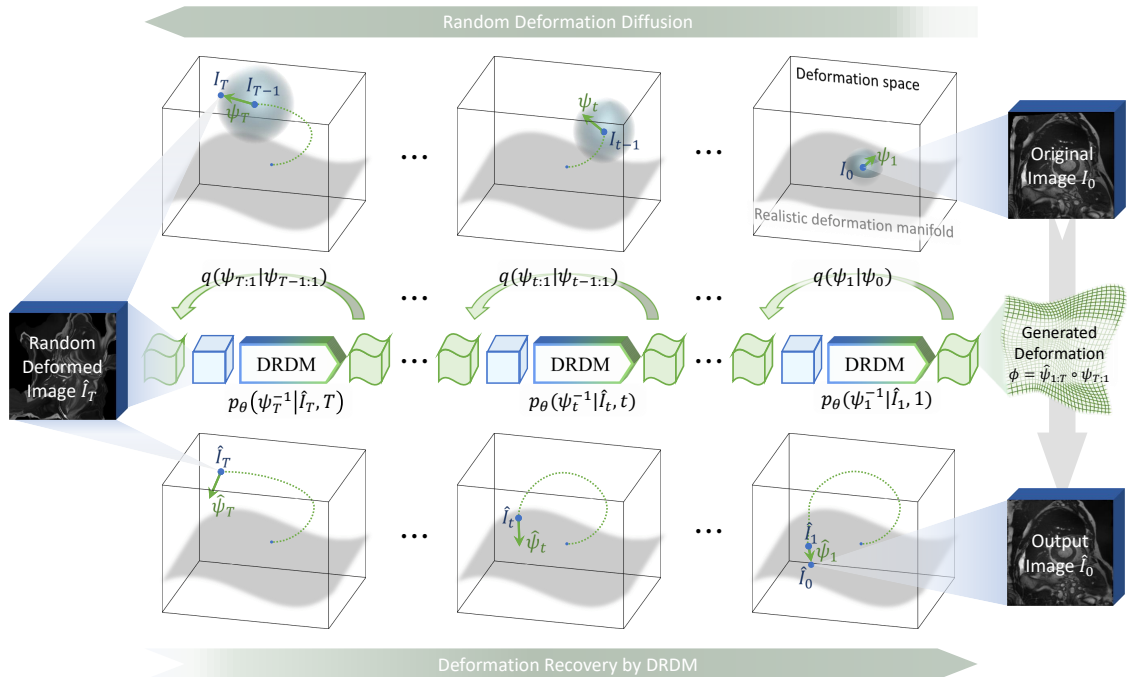


Figure 2: The framework of the DRDM model includes deformation diffusing and recovering processes. The deformation diffusing process is to randomly deform images in the deformation space, and the deformation recovery is to estimate the deformation recursively using DRDM to generate a deformed image in the real deformation manifold.

- Benefiting down-stream tasks:** The experimental results show that data augmentation or synthesis by DRDM improves the downstream tasks, including segmentation and registration. The segmentation method and the registration method based on DRDM respectively outperform the previous augmentation method (Zhang et al., 2020) and the previous synthetic training method (Eppenhof and Pluim, 2019), which validate the plausibility and the value of the deformation field generated by DRDM.

The remainder of the paper is organized as follows. The framework design of DRDM is introduced in Section 2. The experimental setup and the usage of DRDM for generating images and deformation fields are described in Section 3. The application of the generated images with labels for few-shot learning in image segmentation is illustrated in Section 4, and the application of the generated deformation fields and images for synthetic training in image registration is shown in Section 5. Related works are

presented in Section 6. Finally, Section 7 concludes this work.

2. Framework design of DRDM

The framework of DRDM is shown in Figure 2. The generated Dense Displacement Field (DDF) via DRDM is defined as a spatial transformation $\phi : \mathbb{R}^{H \times W \times D} \rightarrow \mathbb{R}^{H \times W \times D}$, represented by corresponding a series of displacement vectors denoted by $\phi[\mathbf{x}] \in \mathbb{R}^3$ at the coordinate $\mathbf{x} \in \mathbb{Z}^3$ of an image $I \in \mathbb{R}^{H \times W \times D}$, where $H, W, D \in \mathbb{Z}_+$ denote the image height, width, and thickness respectively. It is easy to derive that, in the case of a 2D image, the coordinate will be a 2-element vector, and the image shape will exclude the depth dimension. Therefore, to simplify the explanation, we will only discuss the calculations for 3D cases in the following sections of this paper.

The generation of plausible DDF ϕ via DRDM can be decomposed to random deformation diffusing-and-

recovering:

$$\begin{aligned}\phi &= \hat{\psi}_{1:T} \circ \psi_{T:1} \\ &= \underbrace{\hat{\psi}_1 \circ \hat{\psi}_2 \cdots \hat{\psi}_T}_{\text{deformation recovery}} \circ \underbrace{\psi_T \circ \psi_{T-1} \cdots \psi_1}_{\text{deformation diffusion}}\end{aligned}\quad (1)$$

where random deformation diffusing, as described in Section 2.1, is to generate a DDF through a fixed Markov process of random DVF generation and integration of the DVFs:

$$\psi_{t:1} := \psi_t \circ \psi_{t-1} \cdots \psi_1 \sim q(\psi_{t:1} | \psi_{t-1:1}) \quad (2)$$

and deformation recovery, as described in Section 2.2, is to estimate the recovering DDF $\hat{\psi}_{t:T}$ with the inverse DVF for each step ψ_t^{-1} estimated as $\hat{\psi}_t$ recursively based on the input of the deformed image \mathbf{I}_t :

$$\begin{cases} \hat{\psi}_{t:T} := \hat{\psi}_t \circ \hat{\psi}_{t+1} \cdots \hat{\psi}_T \\ \hat{\psi}_t \sim p(\psi_t^{-1} | \hat{\mathbf{I}}_t, t) \end{cases} \quad (3)$$

where $\mathbf{I}_0, \mathbf{I}_t$ denote the original image and the randomly deformed image, $\hat{\mathbf{I}}_0, \hat{\mathbf{I}}_t$ denote the synthesized image by DRDM and the deformed image during deformation recovery:

$$\begin{cases} \mathbf{I}_t := \psi_{t:1}(\mathbf{I}_0) \\ \hat{\mathbf{I}}_t := \langle \hat{\psi}_{t+1:T} \circ \psi_{t:1} \rangle(\mathbf{I}_0) \end{cases} \quad (4)$$

where $0 < t \leq T$ denotes the deformation step in diffusion or recovery processing, T denotes the total number of deformation steps for the diffusion and recovery process, and \circ denotes the composition operation, which is calculated by:

$$\langle \phi_1 \circ \phi_2 \rangle[x] := \phi_2[\phi_1[x] + x] + \phi_1[x] \quad (5)$$

to simulate the process of gradual deformation (Vercauteren et al., 2009). This approach differs from the direct addition (and normalization) of denoising components at varying steps in the intensity-based diffusion models (Ho et al., 2020; Song et al., 2020).

The transformation of images by a given deformation field and the composition between two deformation fields are implemented based on the Spatial Transformer Network (STN) (Jaderberg et al., 2015).

2.1. Forward process for random deformation diffusion

This section introduces the forward processing for random deformation diffusion as illustrated in Figure 3. To

randomly create physically possible deformation in medical imaging, the assumptions, and the corresponding rules are set in Section 2.1.1. According to these assumptions, the method of randomly creating the noisy DVF is described in Section 2.1.2. The method of noise-level setting is described in Section 2.1.3. Finally, Section 2.1.4 introduce the integrating of DVF to DDF and the noise-level setting.

2.1.1. The nature of deformation

As previously mentioned, the Gaussian noise added on intensity introduced in the existing diffusion models (Sohl-Dickstein et al., 2015; Ho et al., 2020; Song et al., 2020) is fully independent of each other pixel/voxel, but the deformation of organs typically is not. Therefore, we need to establish rules, limiting the random deformation, to ensure topological consistency and to avoid the loss of anatomical information during the forward process for random deformation diffusion:

1. Randomness: The deformation vector of each position should yield normal distribution $\psi_t[x] \sim \mathcal{N}(0, \sigma_t^2)$;
2. Local dependency: the deformation field of a continuum should be continuous and thus the stochastic regional discontinuity is limited by $\Delta(\psi_t, \Delta x) := \psi_t[x + \Delta x] - \psi_t[x] \sim \mathcal{N}(0, \sigma_t'(\Delta x)^2)$, where $\sigma_t'(\Delta x_1) \geq \sigma_t'(\Delta x_2)$, $\|\Delta x_1\|_\infty > \|\Delta x_2\|_\infty$;
3. Invertibility: the generated deformation of a continuum should be physically invertible: $|\mathbf{J}|_{<0} < \epsilon$;

where Chebyshev distance $\|\cdot\|_\infty$ is used here, $|\mathbf{J}|_{<0}$ denotes the negative determinant ratio of the Jacobian matrix of a deformation field, ϵ denotes a reasonably small positive value to limit the unrealistic deformation, σ_t^2 denotes the deformation variance of DVF ψ_t at the t^{th} time step, and $\sigma_t'^2$ denotes the deformation discontinuity variance of DVF ψ_t .

These rules are simply designed with a focus on the deformation of a single continuum, although in cases of discontinuous deformation of multiple organs or tissues, the situation could be more complicated as previously discussed in (Zheng et al., 2024).

2.1.2. Multi-scale random DVF generation

According to these rules set in Section 2.1.1, the multi-scale random DVF in each time step is synthesized based

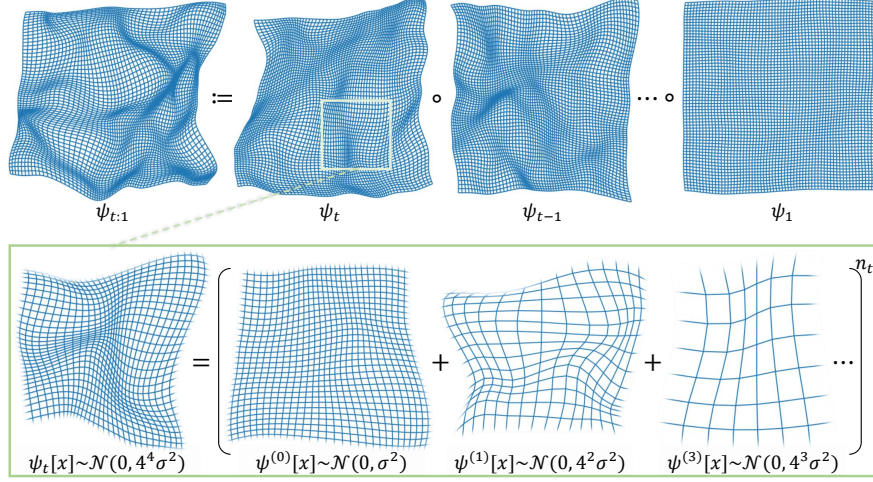


Figure 3: The illustration of the principle for multi-scale random DVF creating and integrating in the deformation diffusion process, as detailed in Equation (2) and (6).

on sampling from multi-scale Gaussian distributions:

$$\left\{ \begin{array}{l} \psi = \psi^{(0)} + \text{intrp}(\psi^{(1)}) + \dots + \text{intrp}(\psi^{(m)}) \\ \psi^{(0)} \in \mathbb{R}^{3 \times h \times w \times d}, \psi^{(0)}[x] \sim \mathcal{N}(0, \sigma^2) \\ \psi^{(1)} \in \mathbb{R}^{3 \times (h/2) \times (w/2) \times (d/2)}, \psi^{(1)}[x] \sim \mathcal{N}(0, (2\sigma)^2) \\ \dots \\ \psi^{(m)} \in \mathbb{R}^{3 \times (h/2^m) \times (w/2^m) \times (d/2^m)}, \psi^{(m)}[x] \sim \mathcal{N}(0, (2^m \sigma)^2) \end{array} \right. \quad (6)$$

where $\text{intrp}(\cdot)$ denotes interpolation of the input image/DDF/DVF to the spatial shape of $h \times w \times d$, $\psi^{(0)}, \psi^{(1)}, \dots, \psi^{(m)}$ denote the independent components of DVF with the original scale, the first-order half-down-sampled scale, \dots and the m^{th} -order half-down-sampled scale. The first rule can be thus satisfied with:

$$\sigma_t^2 \approx \frac{4^{m+1} - 1}{3} \sigma^2 n_t \quad (7)$$

and the second rule can be satisfied by:

$$\sigma_t'^2 \approx 2n_t \sigma^2 \sum_{i=0}^m \min(\|\Delta x\|_\infty, 2^i)^2 \quad (8)$$

where σ^2 denotes the minimum unit of DVF variance, n_t denotes the noise scales for each time step, as described in Section 2.1.3.

2.1.3. Noise scale of the random deformation field

To ensure the invertibility of the generated deformation fields, the DDF is modeled as a pseudo flow, which can be differentiated into a DVF at each time step (diffeomorphism), following the continuum flow method (Christensen et al., 1996). For the sampling of DVF with varying magnitude variance at different time steps, an initial DVF is first sampled with a small fixed variance, and then integrated to a larger DVF with the varying integrating recursion number n_t . The integrating recursion numbers are used to control the magnitude of the random deformation field in the forward process. The noise scaling level is set to increase with the increasing time step t :

$$n_t := t^\alpha / \beta \quad (9)$$

where α and β denote the parameters to control the speed of noise level increase.

2.1.4. Deformation diffusion by integrating DVF to DDF

As described in Equation (2), the created DVF in Section 2.1.2 is then integrated to DDF $\psi_{t:1}$ by composing $\psi_t, \psi_{t-1}, \dots, \psi_1$. Thus the random deformation field $\psi_{t:1}[x] \sim \mathcal{N}(0, \sigma_{t:1}^2)$ can be sampled with:

$$\sigma_{t:1}^2 := \sum_{i=1}^t \sigma_i^2 \approx \frac{4^{m+1} - 1}{3} n_{t:1} \sigma^2 \quad (10)$$

where $n_{t:1}$ denotes the integrated noise scale value:

$$n_{t:1} := \int_1^t n_\tau d\tau \approx \frac{t^{\alpha+1}}{(\alpha+1)\beta} \quad (11)$$

2.2. Reverse process for deformation recovery

Different from the pixel-wise intensity predicted by DDPM or Denoising Diffusion Implicit Model (DDIM) (Ho et al., 2020; Song et al., 2020), the DRDM is used to estimate a deformation field. Figure 4 illustrate the training and usage pipeline of the network for DRDM. The network design for DRDM is introduced in Section 2.2.1. The training method of DRDM is described in Section 2.2.2 and the deformation of instance image using DRDM is described in Section 2.2.3.

2.2.1. Recursive network design for DRDM

As described in Equation (3), the DVF for recovering deformation is estimated and sampled by DRDM \mathcal{D}_θ based on $\hat{\psi}_t \sim p(\psi_t^{-1} | \hat{\mathbf{I}}_t, t)$ with the specific input of image $\hat{\mathbf{I}}_t$ and the time step t :

$$\begin{cases} \hat{\psi}_t^{(0)} : \hat{\mathbf{I}}_t \mapsto \hat{\mathbf{I}}_t \\ \hat{\psi}_t^{(k)} = \mathcal{D}_\theta(\hat{\mathbf{I}}_t^{(k)}, t) \\ \hat{\mathbf{I}}_t^{(k)} = \langle \hat{\psi}_t^{(k-1)} \circ \hat{\psi}_t^{(k-2)} \dots \hat{\psi}_t^{(0)} \rangle(\hat{\mathbf{I}}_t) \\ \hat{\psi}_t = \hat{\psi}_t^{(K)} \circ \hat{\psi}_t^{(K-1)} \dots \hat{\psi}_t^{(1)} \end{cases} \quad (12)$$

where DRDM \mathcal{D}_θ is used to estimate a set of DVF $\hat{\psi}_t^{(k)}$ in the internal recursion $1 \leq k \leq K$ and to integrate them to regress the inverse DVF ψ_t^{-1} .

The U-Net (Ronneberger et al., 2015) architecture is adopted into a recursive structure along with Atrous II block (Zhou et al., 2020) to obtain a larger receptive field, which facilitates a better understanding of spatial features, as advised by (Islam et al., 2019). The detailed network architecture is described in Appendix A.

The internal recursion is designed to ensure that the network can adapt to the input deformed image in a single-step training strategy and K is set to 2 as suggested by (Zheng et al., 2022). It is also worth noting that, in both Equations (4) and (12), multiple deformation fields are composited and applied to input images (\mathbf{I}_0 and $\mathbf{I}_t^{(0)}$) rather than deforming the images for multiple times, in order to avoid blurring deformed images.

Algorithm 1: Training DRDM

Input: Training set of source domain images $\mathbf{D}^{\text{src}} \subset \mathbb{R}^{H \times W \times D}$
Output: DRDM weights θ

```

1 initialize the DRDM parameters  $\theta$ ;
2 while  $\mathcal{L}_{\text{diff}}$  not converge do
    // randomly sample the data
3 sample the original images:  $\mathbf{I}_0 \in \mathbf{D}^{\text{src}}$ ;
4 sample time steps:  $t \sim \mathcal{U}(0, T) \cap \mathbb{Z}$ ;
5 sample random DVFs  $\psi_t$  and DDFs  $\psi_{t:1}$ 
   according to (6), (7) and (10);
   // compute the prediction and the
   loss
6 deform original images from  $\mathbf{I}_0$  to  $\mathbf{I}_t$  using (4);
7 use DRDM  $\mathcal{D}_\theta$  to estimate recovering
   deformation  $\hat{\psi}_t$  via (12);
8 Update gradient descent step  $\nabla_\theta \mathcal{L}_{\text{diff}}$  via (14);
end
9 return model weights  $\theta$ .
```

2.2.2. Network optimizing for DRDM

The DRDM \mathcal{D}_θ is trained for randomly sampled time step $t \sim \mathcal{U}(0, T) \cap \mathbb{Z}$ with the trainable parameters θ optimized by:

$$\min_{\theta} \{ \mathcal{L}_{\text{diff}}(\psi_t, \hat{\psi}_t) \} \quad (13)$$

where the loss function $\mathcal{L}_{\text{diff}}$ is calculated by:

$$\begin{cases} \mathcal{L}_{\text{diff}}^{\text{dist}} := \mathbb{E}_{x, \psi_t, \mathbf{I}_0} (\lambda_1 \mathcal{L}_{\text{diff}}^{\text{dist}} + \lambda_2 \mathcal{L}_{\text{diff}}^{\text{ang}} + \lambda_3 \mathcal{L}_{\text{diff}}^{\text{reg}}) \\ \mathcal{L}_{\text{diff}}^{\text{dist}} := \frac{\|\langle \psi_t \circ \hat{\psi}_t \rangle[x]\|_2}{\|\psi_t[x]\|_2 + \epsilon} \\ \mathcal{L}_{\text{diff}}^{\text{ang}} := -\frac{\psi_t[x]^T \hat{\psi}_t[x + \psi_t[x]]}{\|\psi_t[x]\|_2 \|\psi_t(\hat{\psi}_t[x])\|_2 + \epsilon} \\ \mathcal{L}_{\text{diff}}^{\text{reg}} := \|\nabla_x \hat{\psi}_t[x]\|_1 + \text{relu}(-\det(\nabla_x \hat{\psi}_t[x])) \end{cases} \quad (14)$$

where $\det(\cdot)$ denotes the determinant value of a matrix, $\nabla \hat{\psi}_t$ denotes the Jacobian matrix of the estimated DVF, loss function for training the DRDM model consists of three loss terms, including the distance error loss term $\mathcal{L}_{\text{diff}}^{\text{dist}}$, the angle error loss term $\mathcal{L}_{\text{diff}}^{\text{ang}}$, and the regularization term $\mathcal{L}_{\text{diff}}^{\text{reg}}$, respectively with the three weights $\lambda_1, \lambda_2, \lambda_3$. As shown in Figure 4(a), $\mathcal{L}_{\text{diff}}^{\text{dist}}$ and $\mathcal{L}_{\text{diff}}^{\text{ang}}$ are calculated to evaluate the distance errors and angular errors between each pair of randomly synthesized DVF $\psi_t[x]$ and the corresponding estimated DVF $\hat{\psi}_t[x + \psi_t[x]]$, and $\mathcal{L}_{\text{diff}}^{\text{reg}}$ consist

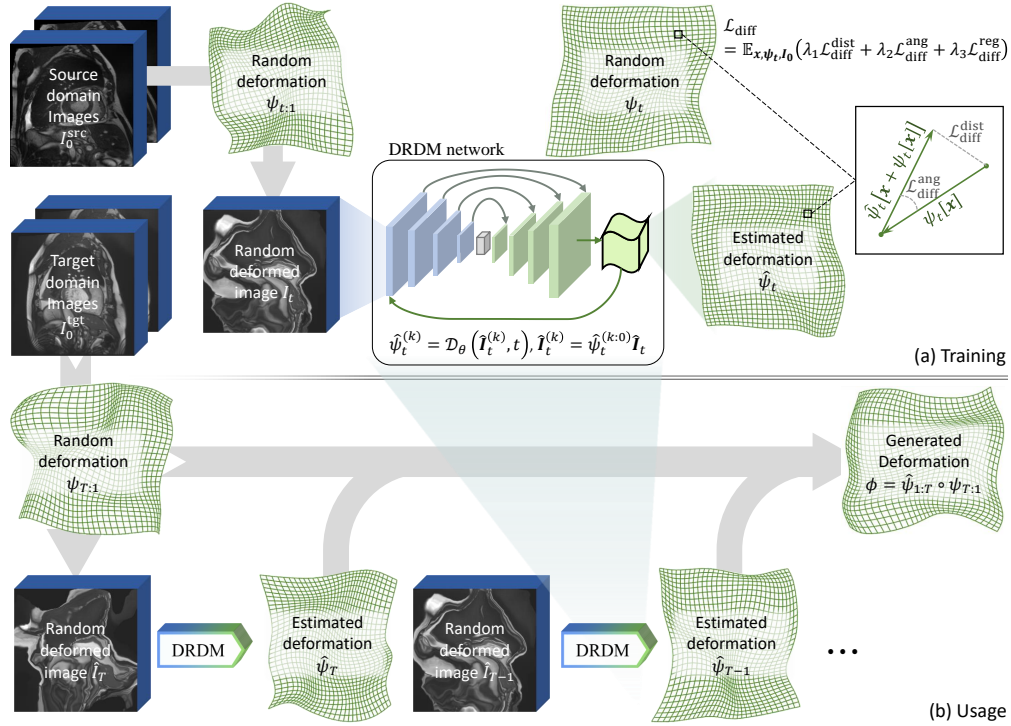


Figure 4: (a) DRDM is trained with each time step using distance- and angle-based loss function, according to Algorithm 1. (b) the deformation fields are estimated with varying time step by the trained DRDM and integrated to generate the final deformation ϕ according to Algorithm 2.

of the regularization terms based on the L1-norms and the negative determinant values of the Jacobian matrices.

As shown in Algorithm 1, the weights of DRDM θ are trained based on a set of training images from a source domain ($\mathbf{I}_0 \in \mathbf{D}^{\text{src}} \subset \mathbb{R}^{H \times W \times D}$). The process begins by initializing the DRDM parameters. It then enters a loop that continues until the loss function $\mathcal{L}_{\text{diff}}$ converges. Within this loop, time steps t are sampled from a uniform distribution, and DVF (ψ_t) and DDFs ($\psi_{t,1}$) are generated as per specified equations. The original images are then deformed to new states (\mathbf{I}_t), and the DRDM estimates the deformation ($\hat{\psi}_t$) necessary to recover the original image state. The model parameters (θ) are updated through gradient descent to minimize the loss $\mathcal{L}_{\text{diff}}$, improving the model’s deformation understanding and recovering capabilities. The training ends when the optimized weights (θ) are finalized upon convergence of the loss function.

2.2.3. Instance deformation synthesis by DRDM

After optimizing the DRDM, the deformation field DDF ϕ is generated based on Algorithm 2, as shown in Figure 4(b). The algorithm is designed to generate a DDF through a sequence of DVFs produced by the trained DRDM \mathcal{D}_θ . Starting with an initial image from the target domain, represented as $\mathbf{I}_0 \in \mathbf{D}^{\text{tgt}}$, with the size of height H , width W , and depth D , the algorithm employs a series of steps to achieve the deformation.

Initially, the algorithm sets a specified deformation step level T' , which must not exceed the maximum step level T , and samples a random DDF $\psi_{T',1}$ based on predefined multi-scale DVF synthesis Equation (6) and (10). This sampled DDF is set as the initial DDF ϕ for the following deformation recovery process.

The image \mathbf{I}_0 undergoes an initial deformation to become $\mathbf{I}_{T'}$, and this image is then set as the initial state for deformation recovery, $\hat{\mathbf{I}}_{T'}$. The core of the algorithm in-

Algorithm 2: Instance Deformation via DRDM

Input: Images for deformation $I_0 \in \mathbb{R}^{H \times W \times D}$ **Output:** Generated DDF ϕ

- 1 import the DRDM parameters θ from Algorithm 1;
 - 2 set the deformation level $T' \leq T$;
// deformation diffusion process
 - 3 sample a random DDF $\psi_{T':1}$ using (6) and (10);
 - 4 set the initial DDF for deformation recovery:
 $\phi \leftarrow \psi_{T':1}$;
 - 5 deform original images from I_0 to $I_{T'}$ using (4);
 - 6 set the initial image for deformation recovery:
 $\hat{I}_{T'} \leftarrow I_{T'}$;
// deformation recovery process
 - 7 **for** $t = T', T' - 1, \dots, 1$ **do**
 - 8 use DRDM \mathcal{D}_θ to estimate recovering deformation $\hat{\psi}_t$ via (12);
 - 9 update the deformation according to (1):
 $\phi \leftarrow \hat{\psi}_t \circ \phi$;
 - 10 deform original images from I_0 to \hat{I}_{t-1} using (4);
 - 11 **end**
 - 12 return the generated deformation ϕ .
-

volves a reverse iteration from $t = T'$ down to 1, where during each iteration, the DRDM estimates the recovering deformation $\hat{\psi}_t$. This estimated deformation is used to progressively update ϕ , integrating the current deformation with the accumulated deformations from previous steps.

Each iteration not only updates the deformation field ϕ but also applies this deformation field to deform I_0 further, resulting in a new image state \hat{I}_{t-1} that progressively deformed from $I_{T'}$. The algorithm concludes by returning the fully generated DDF ϕ , representing the cumulative deformation applied to the original image to reach the final deformed state.

This process, through iterative updating and application of deformations, effectively models complex transformations of the input image, providing a robust method for manipulating image dynamics under the framework of DRDM. The total number of deformation steps T' can be used to control the deformation magnitude from the original image.

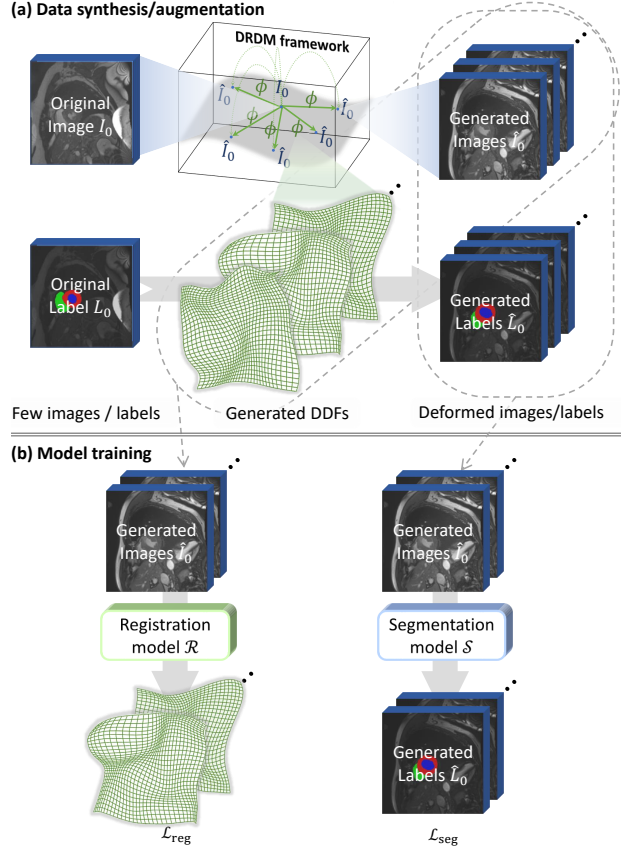


Figure 5: Image and deformation synthesis via DRDM for few-shot learning in image segmentation and image registration. (a) Diverse deformation fields, images, and corresponding labels are generated based on the input few images with labels, as described in Algorithm 3 and Algorithm 4; (b) The generated images and the corresponding labels are used to train a segmentation model, and the generated images with the corresponding DDF are used to train a registration model.

3. Experiment of Image Deformation using DRDM

As shown in Figure 5(a), a few 2D or 3D images are fed into the DRDM framework. The framework then generates deformed images, with or without labels, for downstream tasks as described in the following Section 4 and Section 5. The datasets are divided into a source domain and a target domain. The diffusion networks of DRDM are trained in the source domain and then tested in the target domain for downstream tasks. The datasets used in the experimental implementation of DRDM are described

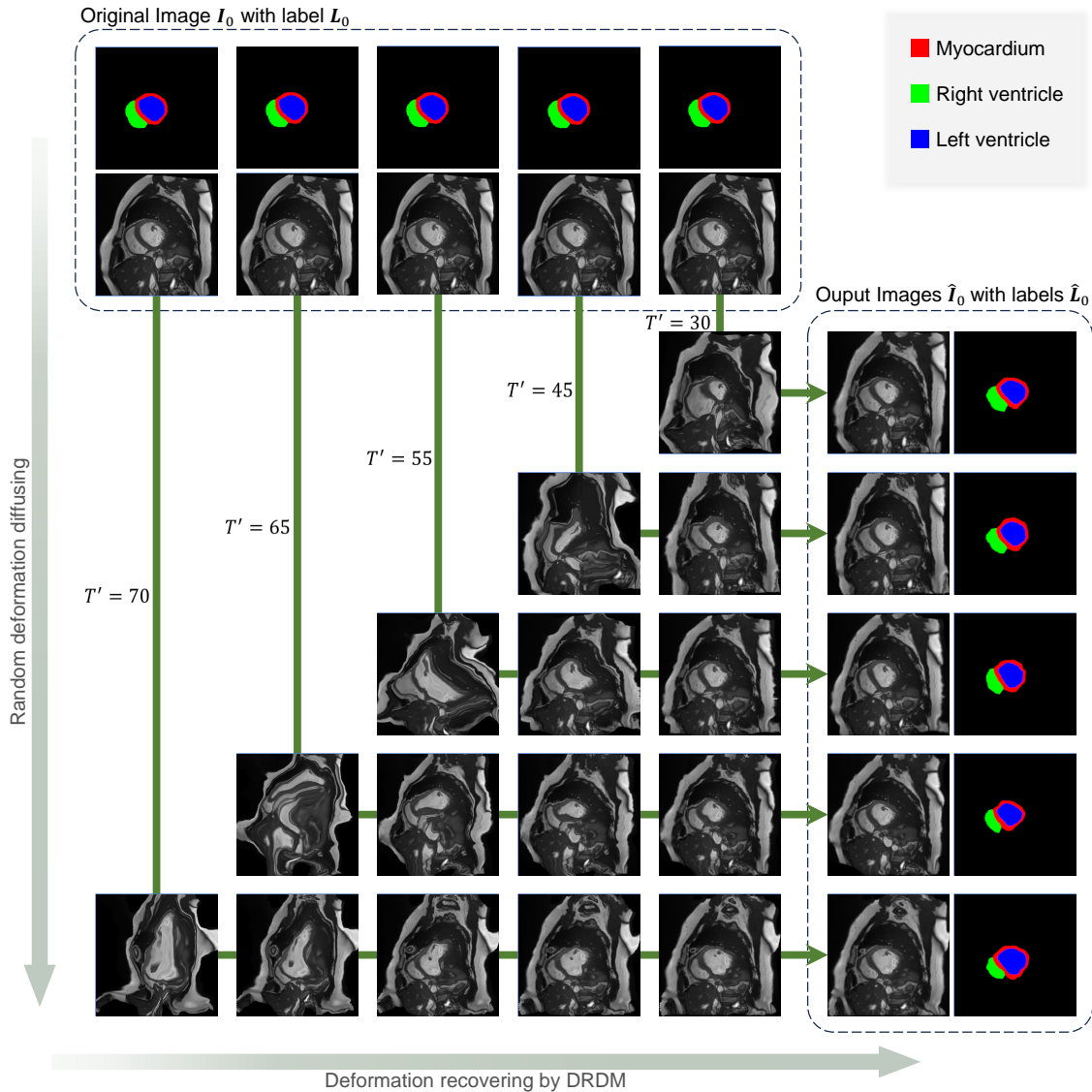


Figure 6: Visualisation of deformation diffusion and recovery for 2D cardiac MRI images via DRDM with varying T' .

in Section 3.1, data processing methods as explained in Section 3.2, set up as detailed in Section 3.3, and the generated data are evaluated in Section 3.4.

3.1. Datasets description

To showcase the effectiveness of the proposed method, we utilized two types of modalities: *Cardiac MRI* and

Thoracic CT scans. The DRDM was trained separately on each of the two modalities and then evaluated on both to verify its deformation performance.

3.1.1. Cardiac MRI

We have gathered 4 different public datasets to construct our training dataset (source domain) and another

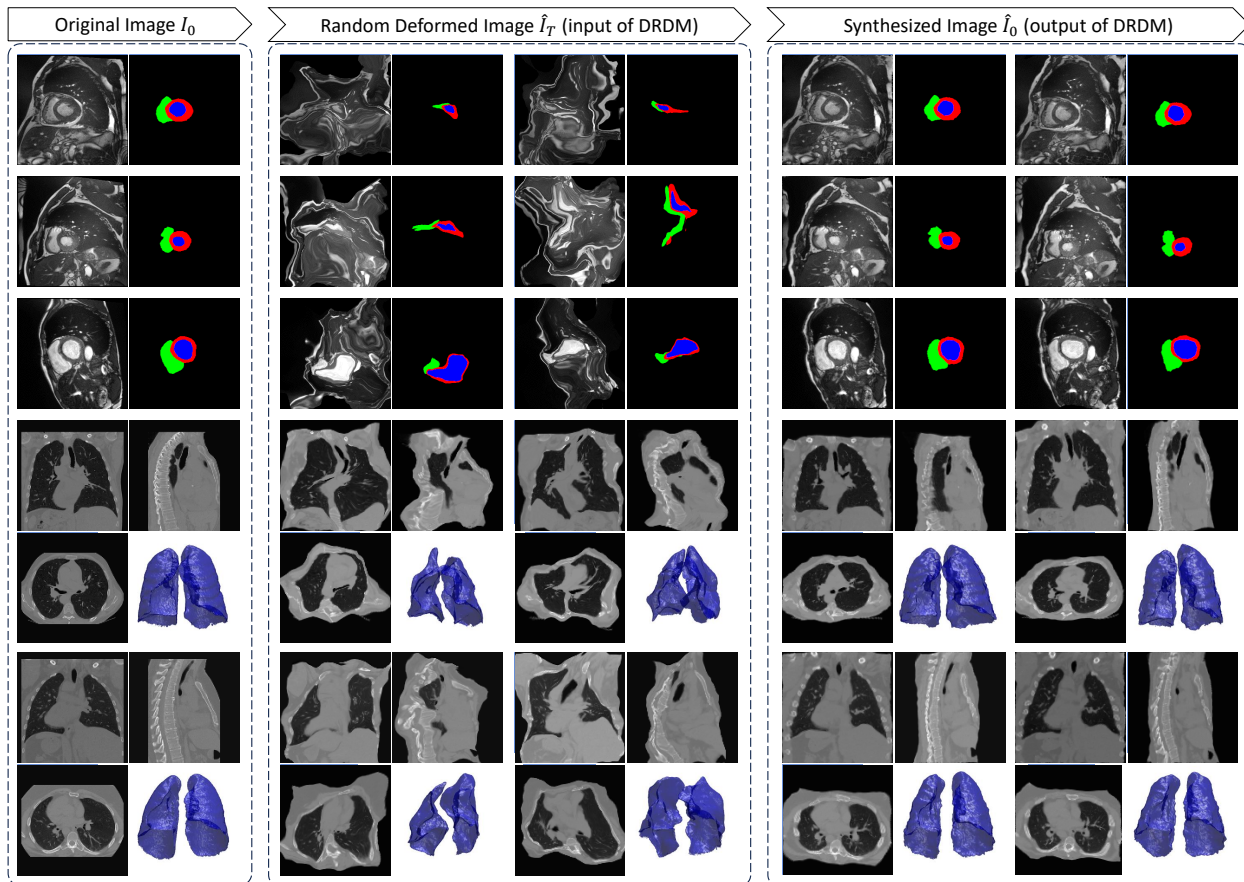


Figure 7: Diverse image deformation for 2D cardiac MRI and 3D pulmonary CT images (cross sections through the center of the image in three directions) via DRDM. Left: the original images, middle: the random deformed images as the input of DRDM, and right: the synthesized images output from DRDM.

Table 1: The average±standard deviation values of the magnitude and the negative determinant ratio of Jacobian ($|J|_{<0}$) of deformation fields with varying deformation level T' in 2D cardiac MRI.

T' (-)	$\max_x \ \phi[x]\ _2$ (%img size)	$\text{avg}_x \ \phi[x]\ _2$ (%img size)	$ J _{<0}$ (%)
30	7.8±1.3	2.4±0.6	0.7±1.5
45	10.4±2.4	3.0±0.8	0.9±1.2
55	11.8±3.2	3.3±0.8	2.4±3.2
65	12.7±4.0	3.6±0.9	6.6±5.5
70	14.8±3.5	4.3±1.4	9.8±7.2

public dataset for the downstream task (target domain) to evaluate DRDM, including:

- The Sunnybrook Cardiac Data (SCD) (Radau et al., 2009) comprises 45 cine-MRI images. These images represent a mix of patients with various conditions: healthy individuals, those with hypertrophy, heart failure with infarction, and heart failure without infarction.
- Task-6 of the Medical Segmentation Decathlon, provided by King’s College London (London, United Kingdom), was originally released as part of the Left Atrial Segmentation Challenge (LASC)

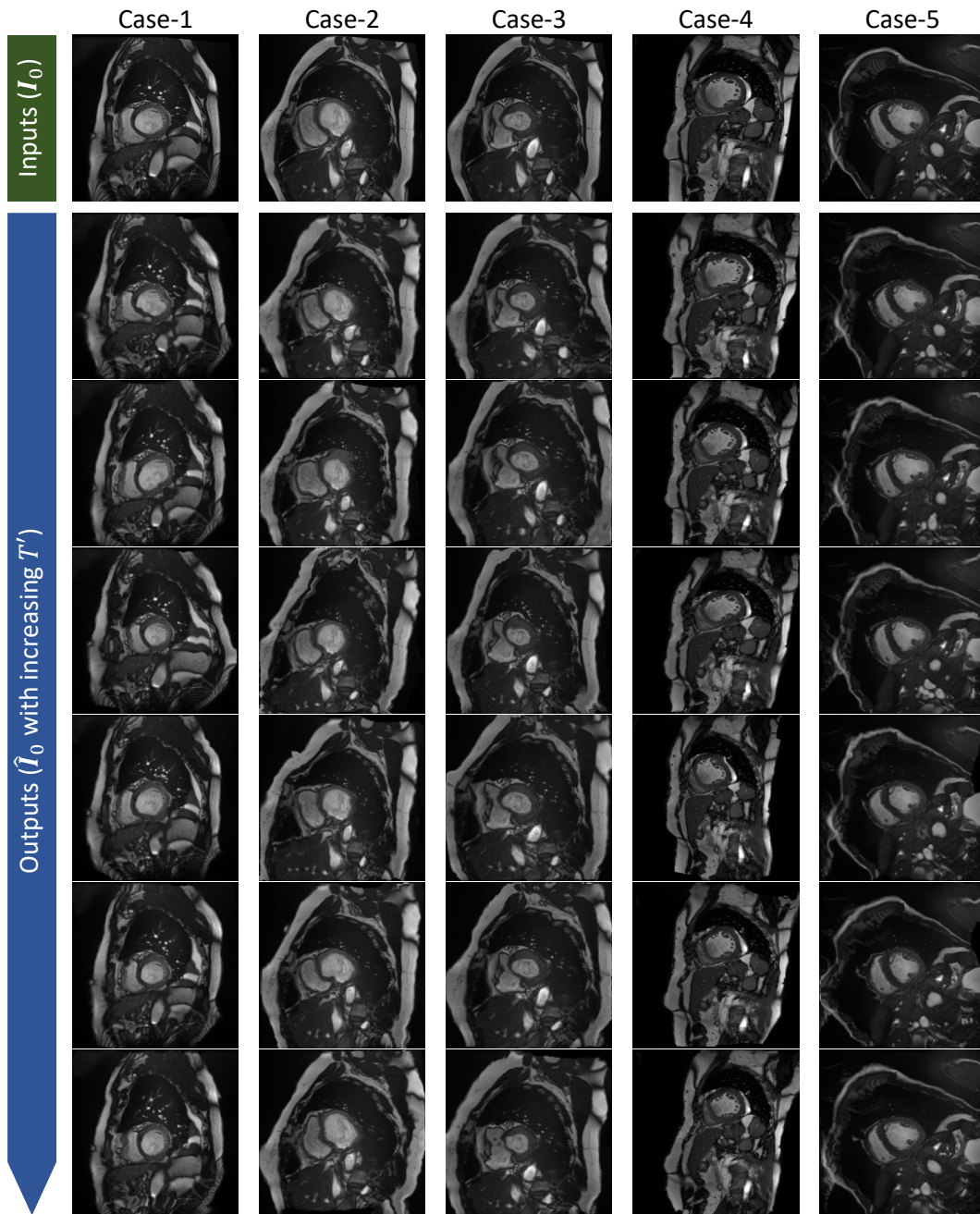


Figure 8: The original and deformed images of five subjects by DRDM for 2D cardiac MRI scans.

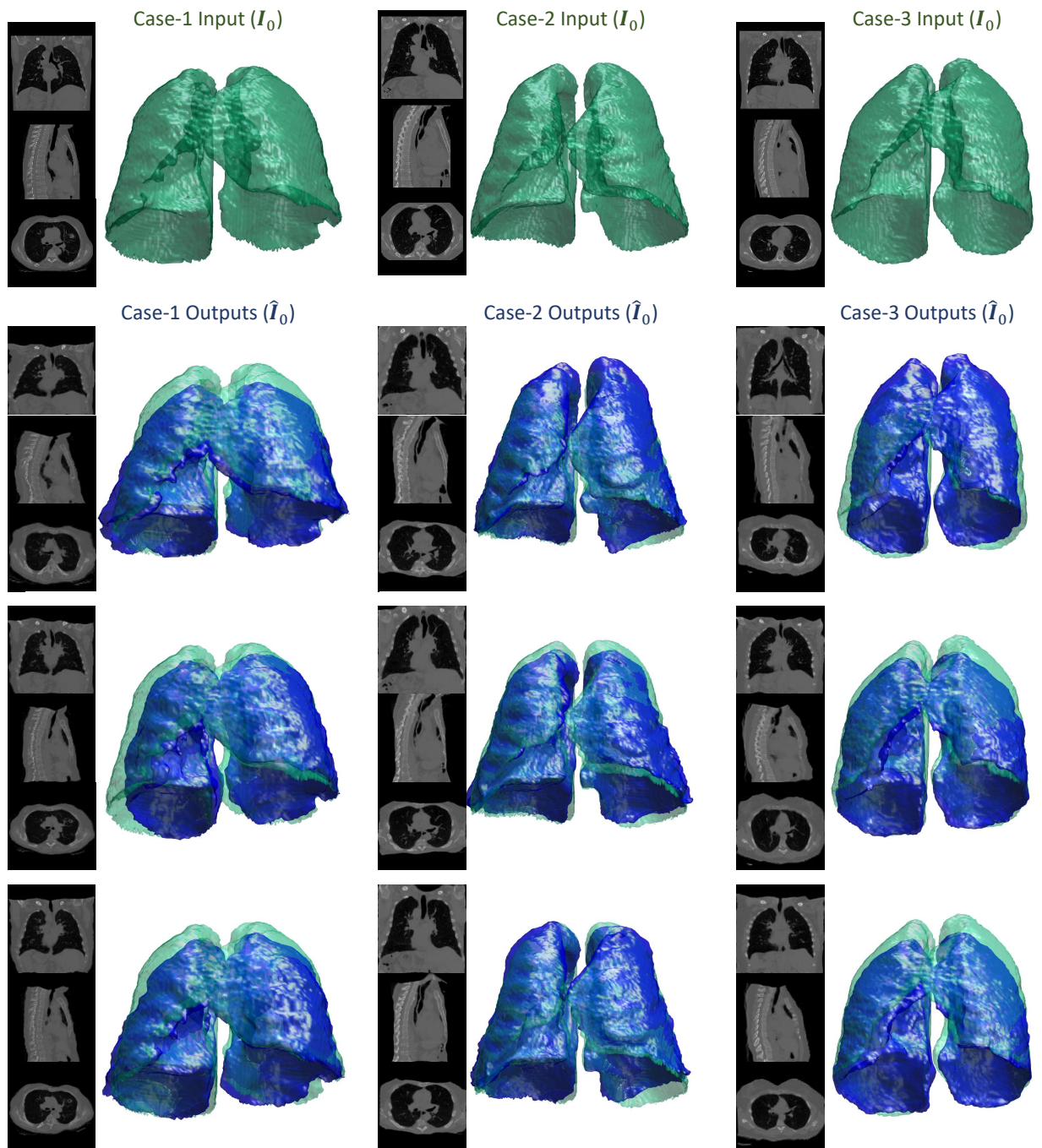


Figure 9: The lung shape and the three cross-sections (frontal, sagittal, and transverse) through the center of the image in three directions for original and deformed images (■ and ■) of three subjects by DRDM for 3D pulmonary CT scans.

- Tobon-Gomez et al. (2015). It includes 30 3D Magnetic Resonance Imaging (MRI) volumes.
- c. The Multi-Centre, Multi-Vendor & Multi-Disease Cardiac Image Segmentation Challenge (M&Ms dataset) (Campello et al., 2021). The challenge cohort included 375 patients with hypertrophic and dilated cardiomyopathies, as well as healthy subjects.
 - d. Multi-Disease, Multi-View & Multi-Center Right Ventricular Segmentation in Cardiac MRI (M&Ms-2 dataset) (Martín-Isla et al., 2023). The challenge cohort consisted of 360 patients with various right ventricle and left ventricle pathologies, as well as healthy subjects.
 - e. For our downstream evaluation task (Whole Heart Segmentation), we used the Automated Cardiac Diagnosis Challenge (ACDC) dataset (Bernard et al., 2018), which consists of cardiac MRI data. It includes 200 cases (100 for training the segmentation model and another 100 for testing).

The datasets a, b, c, and d are used as the source domain data for training of DRDM and the dataset e is used as the target domain data for downstream validation in the segmentation task as described in Section 4.

3.1.2. Thoracic CT

Following a similar approach to Cardiac MRI, we also gathered two public Thoracic CT datasets from the *Cancer Imaging Archive*, along with another public dataset for the downstream task. They are:

- a. NSCLC-Radiomics (Version 4) Aerts et al. (2015), which includes 422 non-small cell lung cancer (NSCLC) patients.
- b. QIN LUNG CT (Version 2) Kalpathy-Cramer et al. (2015), which consists of 47 patients diagnosed with NSCLC at various stages and histologies from the H. Lee Moffitt Cancer Center and Research Institute.
- c. The pulmonary Computer Tomography (CT) scans were provided by Hering et al. (2022) as part of the Learn2Reg 2021 challenge (task 2) dataset. These scans were consistently acquired at the same point within the breathing cycle to ensure uniformity. This dataset includes the inter-subject (exhale) registration task with 20 subjects for the training of a registration model and 10 for testing. Ground truth lung

segmentations are also available for all scans. Each volumetric dataset was prepared with a resolution of $1.75 \times 1.75 \times 1.75 \text{ mm}^3$.

The dataset a and b are used as the source domain data for training of DRDM and the dataset c is used as the target domain data for downstream validation in the inter-subject registration task as described in Section 5.

3.2. Preprocessing and postprocessing

All images are first resized and padded to align with the isotropic resolution size of $H \times W \times D$. Then, the images are thresholded to remove unexpected regions, such as cavity areas. After that, the images’ intensities are linearly normalized to a range of 0-1.

To enhance the robustness of the DRDM network, the images undergo several augmentations: rotating by a random angle $\sim \mathcal{U}(0^\circ, 180^\circ)$ around an arbitrary axis, translating by a random distance $\sim \mathcal{U}(-1/8, 1/8)$ of the image size along each of the three dimensions, randomly flipping with a probability of 0.5, and cropping the cuboid region with a random ratio $\sim \mathcal{U}(0.6, 1.0)$.

After the deformation fields ϕ are generated by DRDM, they are resized to the required size $\tilde{\phi} \in \mathbb{R}^{H' \times W' \times D'}$. As a result, they are applicable to the downstream tasks with required sizes of images or labels.

3.3. Experimental setting for DRDM

In the implementation of the random deformation diffeusing process, the deformation displacement vector out of the field boundary could cause friction against the increase in deformation magnitude. This occurs because the displacement vector out of the sampled size stops accumulating vectors with the "zero" padding mode. To solve this problem, we set a larger size of the deformation field: $h > H$, $w > W$, $d > D$, and then crop the desired deformation field at the centered region $H \times W \times D$ of the created deformation field.

In the experimental implementation of DRDM, H, W, D and H', W', D' are set the same, with 256 for 2D MRI scans and 128 for 3D CT scans. The parameters h, w, d are set as twice the dimensions of H, W, D respectively, and T is set at 80. To increase the robustness of DRDM, a small noisy deformation is introduced during the training process with a 5% disturbance of the created DVF.

The noise level for each time step is set as $n_t := \lfloor t^{0.6} \rfloor$ with $\alpha := 0.6$ and $\beta := 1$. As described in Section 2.1.4, the theoretical setting of the noise level for $\psi_{t:1}$ should be $n_{t:1} = \lfloor t^{1.6}/1.6 \rfloor$, but in practical usage, it is set as $n_{t:1} = \lfloor t^{1.3}/1.5 \rfloor$ to reduce the effects of floor operations and increase the redundancy range of network’s prediction capacity, thus enhancing its ability to recover from random deformation at each step.

The training process uses $\lambda_1 = 1$, $\lambda_2 = 1$, and $\lambda_3 = 10$, with the Adam optimizer. It has an initial learning rate of 0.0001 and batch sizes of 64 for 2D and 4 for 3D. The number of epochs is set to 1000 for the 2D dataset and 2000 for the 3D dataset to ensure the convergence of training. An Intel Xeon(R) Silver 4210R CPU @ 2.40 GHz Central Processing Unit (CPU) and an Nvidia Quadro RTX 8000 Graphics Processing Unit (GPU) with 48 GB of memory are used for parallel acceleration in training.

3.4. Image and deformation synthesis results

The process example of deformation diffusion and recovery in cardiac MRI is illustrated in Figure 6. It shows that the deformation becomes larger with increasing deformation level T' . More image synthesis examples in cardiac MRI and pulmonary CT are shown in Figure 7. It shows diverse images can be synthesized from a few of MRI and CT images in both 2D and 3D. Further examples of the diverse synthesized images by DRDM are presented in Figure 8 for 2D cardiac MRI and Figure 9 for 3D pulmonary CT scans. These examples highlight the diversity and plausibility of the synthesis results, with baseline methods compared in Appendix B (Figure A.13 (Zhang et al., 2020) and Figure A.14 (Eppenhof and Pluim, 2019)).

The quantitative evaluation of the generated deformation is further recorded in Table 1. The maximal and average magnitude of the deformation field is evaluated in the unit of ratio of the image size. The ratio of the negative Jacobian determinant of the deformation is also used to evaluate the rationality of the generated DDF. The results in Table 1 show the ratio of the negative Jacobian determinant ($\mathbb{E}_x \det J_{<0}(\phi)$) and the magnitude ($\max_x \|\phi[x]\|_2$ and $\mathbb{E}_x \|\phi[x]\|_2$) of the generated deformation fields both increase with the larger deformation level T' . But the deformation quality is still relatively high ($\mathbb{E}_x \det J_{<0}(\phi) < 1\%$) even with a large deformation magnitude ($\max_x \|\phi[x]\|_2 > 10\% \times H, W$).

Algorithm 3: Data augmentation via DRDM

Input: Images and labels for deformation
 $\mathbf{D}^{\text{gt}} \subset \mathbb{R}^{H \times W \times D} \times \mathbb{R}^{H \times W \times D \times C}$

Output: Deformed pairs of image and label
 $\mathbf{D}^{\text{aug}} \subset \mathbb{R}^{H \times W \times D} \times \mathbb{R}^{H \times W \times D \times C}$

```

1 import the DRDM parameters  $\theta$  from Algorithm 1;
2 set a set of deformation levels  $\mathcal{T} \subset \mathbb{Z}_+ \cap [1, T]$ ;
3 initialise the output set  $\mathbf{D}^{\text{aug}} \leftarrow \emptyset$ ;
  // sample a pair of image and label
4 foreach  $(\mathbf{I}_0, \mathbf{L}_0) \in \mathbf{D}^{\text{gt}}$  do
  // sample a deformation level number
5   foreach  $T' \in \mathcal{T}$  do
6     generate DDF  $\phi$  using Algorithm 2;
7     deform the sampled image:  $\hat{\mathbf{I}} \leftarrow \phi(\mathbf{I}_0)$ ;
8     deform the sampled label:  $\hat{\mathbf{L}} \leftarrow \phi(\mathbf{L}_0)$ ;
9     append the deformed image and label into
       the output set:  $\mathbf{D}^{\text{aug}} \leftarrow \mathbf{D}^{\text{aug}} \cup \{(\hat{\mathbf{I}}, \hat{\mathbf{L}})\}$ ;
  end
end
10 return the output set  $\mathbf{D}^{\text{aug}}$ .
```

4. Downstream application in image segmentation

Following Figure 5(b), the generated images with the corresponding labels can be used for training a segmentation model \mathcal{S} . Therefore, DRDM is validated in this section as a data augmentation tool for few-shot learning of the image segmentation task. The segmentation framework is described in Section 4.1, with the training process described in Section 4.2. The experimental setup and the corresponding results are respectively explained in Section 4.3 and Section 4.4.

4.1. Segmentation framework

In the segmentation framework, the segmentation masks of specific tissues or regions of pixels/voxels \mathbf{L} are estimated by a segmentation network \mathcal{S}_ζ from a given image \mathbf{I} :

$$\mathcal{S}_\zeta : \mathbb{R}^{H \times W \times D} \rightarrow \{0, 1\}^{H \times W \times D \times C}, \mathbf{I} \mapsto \tilde{\mathbf{L}} \quad (15)$$

with the trainable parameters ζ optimized by:

$$\min_{\zeta} \{\mathcal{L}_{\text{seg}}(\mathbf{L}, \tilde{\mathbf{L}})\} \quad (16)$$

where c denotes the channel number, \tilde{L} denotes the segmentation prediction.

The most commonly used segmentation network structure, U-Net (Ronneberger et al., 2015), is used as the segmentation method in this experiment.

With the U-Net, the dense block consists of two 3×3 convolutions, each followed by a Rectified Linear Unit (ReLU). Max-pool block has one max pooling operation and un-pool block has one up sampling operation both with stride 2. At the end of the network, Sigmoid is used as the output function.

4.2. Segmentation network optimisation

The segmentation loss function \mathcal{L}_{seg} is based on Binary Cross Entropy (BCE):

$$\begin{cases} \mathcal{L}_{\text{seg}} := \mathbb{E}_x \left(\sum_{i=1}^C \mathcal{L}_{\text{seg}}^{\text{bce}}(\mathbf{L}[x, i], \tilde{\mathbf{L}}[x, i]) \right) \\ \mathcal{L}_{\text{seg}}^{\text{bce}} := \mathbf{L}[x, i] \log(\tilde{\mathbf{L}}[x, i]) + (1 - \mathbf{L}[x, i]) \log(1 - \tilde{\mathbf{L}}[x, i]) \end{cases} \quad (17)$$

The training process uses the Adam optimizer with an initial learning rate of 0.001 with the Exponential Learning Rate scheduling. It has batch sizes of 64 for 2D and xxx for 3D. The same CPU and GPU as Section 3.3 in training.

4.3. Experimental setup for segmentation

Using DRDM in this segmentation framework, the original images and corresponding labels from the target domain are augmented with varying deformation level T' as shown in Figure 5(b), which are included in the training data.

To validate the application value of DRDM in segmentation, multiple data augmentation methods are compared in this segmentation framework. Zhang et al. (2020) propose a data augmentation method, named BigAug, including 9 varying stacked transformation modules to change image quality, image appearance, and spatial transform (including deformation) for domain generalization, which has been used as the comparison baseline.

As described in Section 3.1, the ACDC data are split into 100 subjects for training and another 100 for testing. In the experiment of image segmentation, the data are augmented 32 times respectively by DRDM as described in Algorithm 3, and by BigAug (Zhang et al.,

2020). They are compared based on varying labeled training datasets with 5 subjects (5%), 20 subjects (20%), 50 subjects (50%), and 100 subjects (100%).

Multiple metrics are used to evaluate the segmentation models trained based on varying data augmentation methods, including Average Surface Distance (ASD), Dice Similarity Coefficient (DSC) (F1-score), precision (F0-score), and sensitivity (F_{∞} -score) between the labeled segmentation masks \mathbf{L} and the estimated segmentation results $\tilde{\mathbf{L}}$.

Groundtruth label field images were created where 0, 1, 2 and 3 represent voxels located in the background, in the RV cavity, in the myocardium, and in the LV cavity.

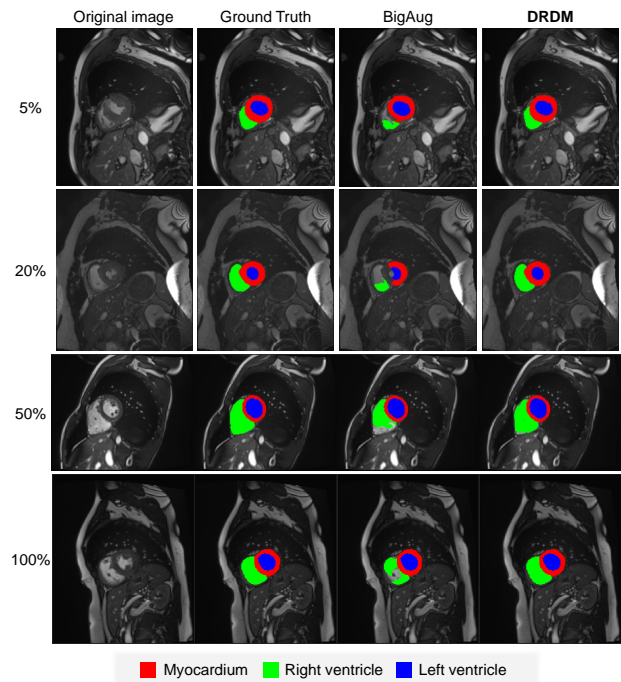


Figure 10: Segmentation examples of segmentation model trained by varying ratio of labeled data, comparing different augmentation methods based on BigAug and DRDM.

4.4. Image segmentation results

The exemplar results of the segmentation experiment in cardiac MRI are shown in Figure 10, with varying ratios of labeled data at 5%, 20%, 50%, and 100%. These

Table 2: Segmentation results of average DSC (%), sensitivity (sns/%), and precision (prec/%) on cardiac MRI by different data augmentation methods based on training a vanilla U-Net with varying subjects number (#subj) and ratio of the labeled images.

#subj /ratio	aug method	Left ventricle			Right ventricle			Myocardium			Average		
		dsc↑	sns↑	prec↑	dsc↑	sns↑	prec↑	dsc↑	sns↑	prec↑	dsc↑	sns↑	prec↑
5 / 5%	N/A	55.0	77.5	45.5	39.5	48.9	35.6	46.3	63.9	39.0	46.9	63.4	40.0
	BigAug	75.8	73.6	83.2	37.6	29.6	65.2	65.6	66.0	69.1	59.7	57.7	72.5
	DRDM	77.0	73.7	84.1	59.6	55.8	77.3	67.9	68.5	73.4	68.2	66.0	78.3
20 / 20%	N/A	75.8	83.7	72.8	59.7	52.6	74.9	62.1	63.7	66.8	65.8	66.6	71.5
	BigAug	78.0	75.3	85.5	53.9	47.1	79.9	68.9	64.1	81.6	66.9	62.2	82.3
	DRDM	83.0	86.8	81.4	75.0	75.6	78.9	74.6	82.5	71.8	77.5	82.6	77.4
50 / 50%	N/A	82.9	80.6	83.0	70.2	65.1	83.3	74.6	77.9	72.7	75.9	74.5	79.7
	BigAug	84.8	83.1	90.3	61.1	54.5	84.9	78.5	77.1	82.8	74.8	71.6	86.0
	DRDM	91.4	95.5	88.3	85.6	89.8	83.5	84.1	94.4	88.3	87.1	93.2	86.7
100 / 100%	N/A	89.3	90.5	92.6	85.2	83.2	89.4	84.9	83.8	86.9	86.5	85.8	89.6
	BigAug	87.2	80.2	97.6	76.9	69.3	92.7	81.5	79.8	85.0	81.9	76.4	91.8
	DRDM	92.5	96.5	89.1	87.9	93.2	83.8	85.4	95.1	77.8	88.6	94.9	83.6

qualitative results demonstrate that the U-Net model augmented with our DRDM outperforms the BigAug approach, particularly in the right ventricle.

The distribution of DSC and ASD values are plotted in Figure 11 for further quantitative comparison. The results indicate that our DRDM method outperforms BigAug across most label ratio settings. Specifically, the DSC and ASD metrics for our DRDM are significantly higher than those for BigAug in the right ventricle and generally higher in the other two tissues ($p < 0.01$).

The numerical averages for DSC, sensitivity, and precision are presented in Table 2. These results consistently show that our DRDM outperforms BigAug in most settings for DSC and sensitivity (sns). It is worth noting that BigAug tends to conservatively segment tissue regions, as shown in Figure 10. This approach results in higher precision values but also increases the false negative prediction rate, thereby reducing sensitivity.

5. Downstream application in image registration

Following Figure 5(b), the generated images with the corresponding DDF can be used for pre-training a registration model \mathcal{R} . Therefore, DRDM is also validated in this section as a data synthesis tool for synthetic training

of the image registration task. The segmentation framework is described in Section 5.1, with the training process described in Section 5.2. The experimental setup and the corresponding results are respectively explained in Section 5.3 and Section 5.4.

5.1. Registration framework

In the registration framework, the deformation field between a pair of images is estimated by a registration network \mathcal{R}_η :

$$\mathcal{R}_\eta : (\mathbb{R}^{H \times W \times D}, \mathbb{R}^{H \times W \times D}) \rightarrow \mathbb{R}^{H \times W \times D \times 3}, (\mathbf{I}^{\text{mv}}, \mathbf{I}^{\text{fx}}) \mapsto \tilde{\phi} \quad (18)$$

with the trainable parameters η optimized by:

$$\min_{\eta} \{\mathcal{L}_{\text{reg}}(\mathbf{I}^{\text{mv}}, \mathbf{I}^{\text{fx}}, \tilde{\phi})\} \quad (19)$$

where $\mathbf{I}^{\text{mv}}, \mathbf{I}^{\text{fx}}$ denotes the moving image as the starting and the fixed image as the target image of the registration, and $\tilde{\phi}$ denotes the estimated deformation field.

The most commonly used registration model, VoxelMorph (Balakrishnan et al., 2019), is used as the network structure in this experiment.

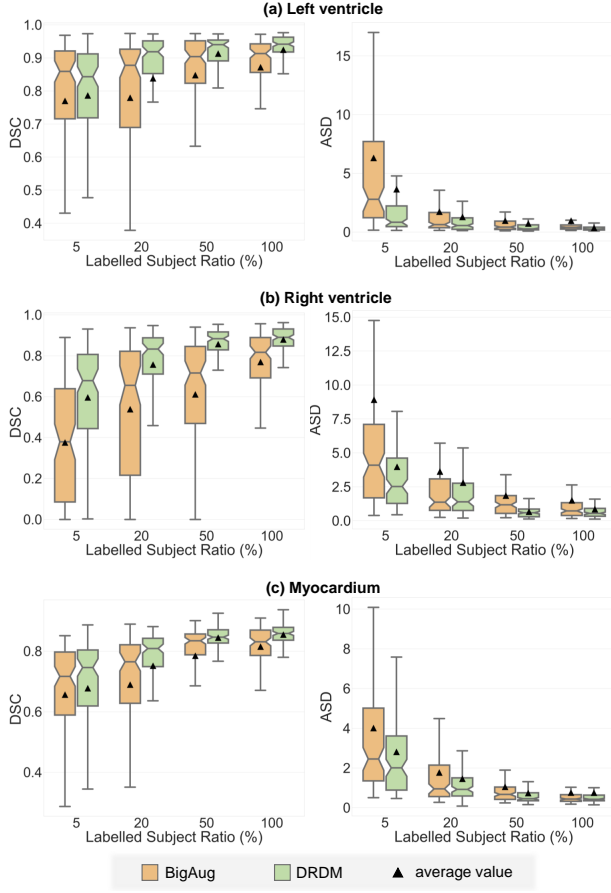


Figure 11: Quantitative results of segmentation model trained by the varying ratio of labelled data, comparing DRDM and others within three organs in cardiac MRI. It shows our method outperforms the baseline in different settings of labelled data.

5.2. Registration network optimisation

The registration network is pre-trained by synthetic images and the corresponding deformation field, which are synthesized by using DRDM, with varying deformation levels T' . The pre-trained registration loss function \mathcal{L}_{reg} consists of two components, Mean Square Error (MSE) and smoothing term:

$$\begin{cases} \mathcal{L}_{\text{reg}} := \lambda_4 \mathcal{L}_{\text{reg}}^{\text{mse}} + \lambda_5 \mathcal{L}_{\text{reg}}^{\text{grad}} \\ \mathcal{L}_{\text{reg}}^{\text{mse}} := \mathbb{E}_x(\|\phi - \tilde{\phi}\|_2) \\ \mathcal{L}_{\text{reg}}^{\text{grad}} := \mathbb{E}_x(\|\nabla \tilde{\phi}[x]\|_1) \end{cases} \quad (20)$$

Algorithm 4: Data synthesis via DRDM

Input: Images for deformation $\mathbf{D}^{\text{tgt}} \subset \mathbb{R}^{H \times W \times D}$

Output: Pairs of deformed images and the DDF

$$\mathbf{D}^{\text{syn}} \subset \mathbb{R}^{H \times W \times D} \times \mathbb{R}^{H \times W \times D} \times \mathbb{R}^{H \times W \times D \times 3}$$

```

1 import the DRDM parameters  $\theta$  from Algorithm 1;
2 set a set of deformation levels  $\mathcal{T} \subset \mathbb{Z}_+ \times \mathbb{Z}_+$ ;
3 initialise the output set  $\mathbf{D}^{\text{syn}} \leftarrow \emptyset$ ;
  // sample an image
4 foreach  $I_0 \in \mathbf{D}^{\text{tgt}}$  do
  // sample deformation level numbers
5   foreach  $(T'_{\text{aug}}, T'_{\text{syn}}) \in \mathcal{T}$  do
6     // create the moving image
7     generate DDF  $\phi_{\text{aug}}$  based on  $(I_0, T'_{\text{aug}})$ 
8     using Algorithm 2;
9     deform the sampled image:
10     $I^{\text{mv}} \leftarrow \phi_{\text{aug}}(I_0)$ ;
11    // create the fixed image and DDF
12    generate DDF  $\phi_{\text{syn}}$  based on  $(I^{\text{mv}}, T'_{\text{syn}})$ 
13    using Algorithm 2;
14    deform the sampled image:
15     $I^{\text{fx}} \leftarrow \langle \phi_{\text{syn}} \circ \phi_{\text{syn}} \rangle(I_0)$ ;
16    append the deformed images and the DDF:
17     $\mathbf{D}^{\text{aug}} \leftarrow \mathbf{D}^{\text{syn}} \cup \{(I^{\text{mv}}, I^{\text{fx}}, \phi_{\text{syn}})\}$ ;
18  end
19 end
20 return the output set  $\mathbf{D}^{\text{syn}}$ .

```

After that, the pre-trained registration models are fine-tuned by the optimizing method following (Balakrishnan et al., 2019).

The synthetic training process uses $\lambda_4 = 1$ and $\lambda_5 = 1$, with the Adam optimizer. It has an initial learning rate of 0.0001 and batch sizes of 12. The same CPU and GPU as Section 3.3 in training.

5.3. Experimental setup for registration

As previously described in Section 3.1, the pulmonary CT data provided by (Hering et al., 2022) is split into 20 for training and 10 for testing.

As described in Algorithm 4, the original images are first augmented by DRDM as the moving images I^{mv} , and then deformed by DRDM as the fixed images I^{fx} with the

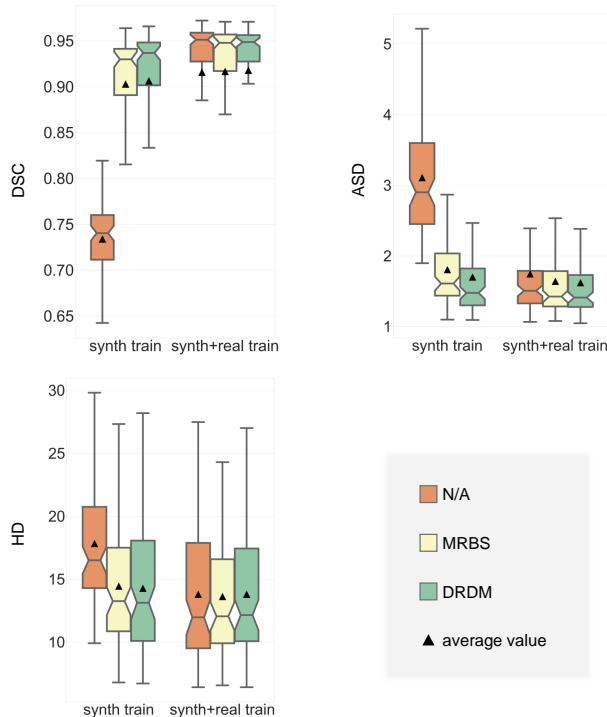


Figure 12: Quantitative results of registration models with synthetic training and real training, validating the improvement from pre-trained via DRDM.

given deformation field ϕ between, which are used as the synthetic training data.

To validate the application value of DRDM in registration, the synthetic training methods (Eppenhof and Pluim, 2019) based on a multiple-resolution B-spline (MRBS) method is compared in this registration framework, following the original setting described in (Eppenhof and Pluim, 2019).

Following the setting of (Eppenhof and Pluim, 2019), in the experiment of image registration, the training data are first augmented respectively (20 CT scans \times 32), and then the deformation fields to be learned are synthesized by DRDM or B-spline transformer.

After synthetic training, the registration models are further unsupervised-finetuned based on the real data following (Balakrishnan et al., 2019)

Multiple metrics are used to evaluate the data augmentation methods in segmentation performance, including

DSC (F1), ASD, and Hausdorff Distance (HD) between the labeled masks of the lung in the fixed image L and the mask of the lung deformed by the estimated deformation field \tilde{L} .

Table 3: Inter-subject registration results of average DSC (%), ASD (voxel), and HD (voxel) on pulmonary CT predicted by a vanilla Voxel-Morph (Balakrishnan et al., 2019), with varying synthetic training methods using Multi-Resolution B-Spline (MRBS) (Eppenhof and Pluim, 2019) and our DRDM, following the unsupervised fine-tuning on the real data (real train).

synth method	real train	DSC \uparrow (%)	ASD \downarrow (vox)	HD \downarrow (vox)	$ J _{<0}$ \downarrow (%)
N/A	\times	73.39	3.11	17.82	-
MRBS	\times	90.29	1.80	14.45	3.25
DRDM	\times	90.64	1.71	14.27	4.42
N/A	\checkmark	91.57	1.74	13.80	5.38
MRBS	\checkmark	91.66	1.64	13.62	4.96
DRDM	\checkmark	91.79	1.62	13.71	4.95

5.4. Image registration results

The distribution of DSC, ASD, and HD values evaluated for our model and the baselines are plotted in Figure 12. The registration model synthetically trained by our DRDM method outperforms that by MRBS in ASD ($p < 0.05$). Additionally, the registration model trained synthetically using our DRDM is competitive with the model trained on real data.

The numerical average values of DSC, ASD, HD, and negative Jacobian determinant ratio are presented in Table 3. These results consistently demonstrate that our DRDM significantly outperforms MRBS in synthetic training of the registration model, achieving a performance level comparable to the registration model trained on real data.

These experimental results in the registration task further validate the efficacy of the deformed images generated by our DRDM.

6. Related Works

6.1. Diffusion models in medical image analysis

Multiple previous studies have explored the application of diffusion models in medical image analysis tasks, including anomaly detection Wolleb et al. (2022); Bercea

et al. (2023); Liang et al. (2023) and image registration (Qin and Li, 2023; Gao et al., 2023).

Wolleb et al. (2022) proposed a method that combines an intensity noising-and-denoising scheme (Ho et al., 2020; Song et al., 2020) with classifier guidance for 2D image-to-image translation. This technique transforms images from diseased subjects into their healthy counterparts while preserving anatomical information. The difference between the original and translated images highlights the anomaly regions in brain MRI. Similarly, Bercea et al. (2023) introduced an AutoDDPM method, based on DDPM (Ho et al., 2020), for anomaly detection in brain MRI, incorporating an iterative process of stitching-and-resampling to generate pseudo-healthy images. Additionally, Liang et al. (2023) described MM-CCD for segmenting anomalies across diverse patterns in multimodal brain MRI, utilizing an intensity-based diffusion model (Ho et al., 2020; Song et al., 2020).

Qin and Li (2023) integrated DDPM (Ho et al., 2020) with a registration framework, introducing a feature-wise diffusion-guided module to enhance feature processing during the registration process, and a score-wise diffusion module to guide the optimization process while preserving topology in 3D cardiac image registration tasks. Gao et al. (2023) also employed DDPM (Ho et al., 2020) to facilitate multimodal registration of brain MRI, merging DDPM with a discrete cosine transform module to disentangle structural information, simplifying the multimodal problem to a quasi-monomodal registration task.

In these works, diffusion models typically function as converter models to translate images from one diseased subject to a healthy one or from one modality to another, rather than acting as generative models.

6.2. Diffusion model for medical image synthesis and manipulation

Pinaya et al. (2022) proposed a 3D brain T1w MRI synthesis framework based on a Latent Diffusion Model (LDM) (Rombach et al., 2022), incorporating a DDIM sampler (Song et al., 2020) to condition the generated images on the subject’s age, sex, ventricular volume, and brain volume. Ju and Zhou (2024) combined the advanced Mamba network (Gu and Dao, 2023) with a cross-scan module into the DDPM framework (Ho et al., 2020) to generate medical images, validated on chest X-rays, brain MRI, and cardiac MRI.

Although these methods are capable of generating life-like images, they still face issues such as illusions and the inability to make interpretable connections with existing images. Consequently, these generated images cannot augment data with corresponding annotations for downstream tasks as detailed in Sections 4 and 5.

Generating deformation fields rather than images through diffusion modeling can address this issue. DiffuseMorph, proposed in (Kim et al., 2022), uses DDPM (Ho et al., 2020) as a diffusion module to estimate the conditional score function for deformation, combined with a deformation module to estimate continuous deformation between image pairs for registration tasks, including 4D temporal medical image generation of cardiac MRI (Kim and Ye, 2022). Recently, Starck et al. (2024) introduced a conditional atlas generation framework based on LDM (Rombach et al., 2022), generating deformation fields conditioned on specific parameters, with a registration network guiding the optimization of atlas deformation processes.

However, these methods still rely on diffusion-denoising of intensity (Kim et al., 2022; Kim and Ye, 2022) or hidden-feature (Starck et al., 2024), utilizing registration frameworks to guide and constrain the rationality of generated deformations. Consequently, the diversity of the generated deformations is limited to the interpolation between pairs of images (Kim et al., 2022; Kim and Ye, 2022) or the deformation of atlas images (Starck et al., 2024). This limitation hinders the generation of diverse deformations for individual images and challenges the augmentation of images or the generation of diverse deformation fields for downstream tasks.

6.3. Data augmentation for few-shot image segmentation

Several techniques have been previously proposed for few-shot image segmentation, addressing the challenge of limited annotations in medical image analysis. These methods mainly include pseudo-label-based approaches and data augmentation techniques.

Dang et al. (2022) introduced a few-shot learning framework for vessel segmentation, utilizing weak and patch-wise annotations. This approach includes synthesizing pseudo-labels for a segmentation network and utilizing a classifier network to generate additional labels and assess low-quality images. An uncertainty estimation-based mean teacher segmentation method was

proposed to enhance the reliable training of a student model in cardiac MRI segmentation (Wang et al., 2022b). Another semi-supervised method was introduced based on mutual learning between two Vision Transformers and one Convolutional Network, utilizing a dual feature-learning module and a robust guidance module designed for consistency (Wang et al., 2022a).

However, pseudo-label-based methods require a sufficient number of annotated labels to ensure the accuracy of an additional model for pseudo-label creation, which limits their applicability in tasks with extremely limited annotations.

An atlas-based data augmentation technique is introduced in (Zhao et al., 2019) to create labeled medical images for brain MRI segmentation by spatially and cosmetically aligning an annotated atlas with other images. However, the diversity of the augmented data is limited by the provided total data domain. Additionally, a separate registration model and appearance transform model need to be trained for each new atlas to be used. Bortsova et al. (2019) proposed a few-shot segmentation method based on data augmentation through elastic deformation transform (Davis et al., 1997), with a segmentation consistency loss across labeled and unlabeled images. Furthermore, Zhang et al. (2020) proposed a combination of nine different types of cascaded augmentation methods, named BigAug. These methods vary image quality (sharpness, blurriness, and intensity noise level), image appearance (brightness, contrast, and intensity perturbation), and spatial configuration (rotation, scaling, and deformation), validated on cardiac MRI/ultrasound and prostate MRI. This method, BigAug, has also been compared in Section 4.

Additionally, a data-efficient learning approach was proposed by Mo et al. (2024), involving learning a vector field from the cropped patches of an instance image to trace the boundary of the target tissues. This method achieved impressive performance with extremely limited labeled training data in heart and lung segmentation from chest X-ray and skin lesion from dermoscopy images (Mo et al., 2024). However, it suffers from limitations in segmenting complex topological tissues and is difficult to apply to 3D image data.

6.4. Synthetic training for image registration

There have been previous applications of synthetic spatial transformations for training image registration models. For example, random rigid transformations can be easily synthesized to train a model for rigid registration, aimed at aligning micro-CT scans of murine knees with and without contrast enhancement (Zheng et al., 2023).

Rohé et al. (2017) proposed a training strategy for cardiac MRI deformable registration, based on synthetically deforming the segmented mask of the target tissues via elastic body splines (Davis et al., 1997). Similarly, Uzunova et al. (2017) adopted a locality-based multi-object statistical shape model method (Wilms et al., 2017) for statistical appearance modeling, to synthesize training data for medical image registration. However, these methods rely on segmentation masks or statistical shapes of the target tissues prior to training the registration model, making them unsuitable for unsupervised training approaches.

To avoid the usage of annotations, random deformations based on Gaussian smoothing sampling (Sokooti et al., 2017; Gonzales et al., 2021) have been used for registration model training. More recently, a mixture of Gaussian and thin-plate splines (Zheng et al., 2022, 2024) have also been used for pretraining registration models. For augmentation and synthesis in pulmonary CT registration, B-spline (Lee et al., 1997) has been adopted as a Multi-Resolution version and employed for random deformation generation in (Eppenhof and Pluim, 2019), which have been compared in Section 5.

7. Discussion and Conclusion

7.1. Plausible and diverse deformation synthesis

The experiments conducted on cardiac MRI and pulmonary CT, as described in Section 3, demonstrate that our method, DRDM, can generate plausible and diverse deformations for instance-specific images. Unlike previous deformation methods (Kim et al., 2022; Kim and Ye, 2022; Starck et al., 2024), DRDM does not require a registration framework to guide the deformation, enabling it to create more varied deformations. In comparison to earlier deformation-based augmentation methods (Zhang et al., 2020; Eppenhof and Pluim, 2019), DRDM can produce customized and plausible deformations for each individual image.

7.2. Improvement of downstream task

As described in Section 4 and Section 5, further experiments on segmentation and registration tasks validate the efficacy and applicability of the diverse and instance-specific deformations generated by DRDM. Previous augmentation methods typically rely on fully random transformations in image quality, image appearance, and spatial features, without customization for each individual image. In contrast, DRDM synthesizes more realistic images and thus improves the downstream-task models in learning the realistic distribution of images by balancing diversity and plausibility. It is also noteworthy that DRDM can be combined with other data augmentation methods to further enhance downstream tasks. The success in the downstream tasks also illustrate the reasonableness and effectiveness of the generation output by DRDM.

7.3. Limitations of this research

Our aim is to generate diverse, high-quality, and realistic image deformations. Although experimental results in Section 3 show that the generated deformations are diverse and reasonable, the quality of realism after deformation can only be evaluated subjectively from the images. It is challenging to evaluate this feature quantitatively. This dilemma is common in image generation tasks. While FID (Fréchet Inception Distance) is a commonly used metric to measure the relationship between the generated image distribution and the original distribution in natural image generation tasks (Rombach et al., 2022; Ho et al., 2020; Song et al., 2020; Qiao et al., 2019), but often face problems of misaligned data distribution (Jayasumana et al., 2024) and the scarcity of pre-trained models for usage in medical image synthesis.

Therefore, we rely on the applications of DRDM in downstream tasks, such as segmentation and registration, to demonstrate the quality and clinical utility of the synthesised medical images. The improvement in downstream model tasks can prove that the synthetic images and deformation generated by DRDM conform to the data distributions learned by the segmentation and registration models in the downstream tasks. However, it is important to note that the data distributions learned by these downstream tasks are only indirectly related to the actual real-world data distribution.

7.4. Prospective applications in future

This paper demonstrates the application value of DRDM for data augmentation in few-shot segmentation and data synthesis for registration. There is considerable potential for exploring other directions. The DRDM can be modified with conditional input to regulate the generated deformation fields and thus the deformed images with a desired type. A segmentation module can be employed to decompose different regions of images, enabling DRDM to generate more complex deformation fields with multiple continuums. An image modality converter module can be combined to generate deformed images in another modality. Furthermore, DRDM can be combined with a conventional intensity/score-based or latent-based diffusion model to address the common textural inconsistency problem in the generation of videos or dynamic image scans.

7.5. Conclusion

In this paper, we propose a novel diffusion-based deformation generative model, DRDM, for image manipulation and synthesis. The experimental results indicate that DRDM achieves both rationality and diversity in the generated deformations, and significantly improves downstream tasks such as cardiac MRI segmentation and pulmonary CT registration, demonstrating its great potential in medical imaging and other fields.

8. Acknowledgements

J.-Q. Z. acknowledges the Kennedy Trust Prize Studentship (AZT00050-AZ04) and the Chinese Academy of Medical Sciences (CAMS) Innovation Fund for Medical Science (CIFMS), China (grant number: 2018-I2M-2-002). B.W.P. acknowledges the Rutherford Fund at Health Data Research UK (grant no. MR/S004092/1).

9. Declaration of AI technologies used in writing

During the preparation of this work the authors used ChatGPT¹ in order to proofread the text. After using this

¹OpenAI. (2024). ChatGPT (4o) [Large language model]. <https://chatgpt.com>

tool/service, the author(s) reviewed and edited the content as needed and take(s) full responsibility for the content of the published article.

Appendix A. Network architecture for DRDM

The network structure detail for the DRDM is shown in Table .4, where "embed" denotes feature embedding, "fc" denotes a fully connected layer, "act" denotes the ReLU activation function with 0.01 negative slope, "#chnl" denotes channel number for input or output, "conv" denotes the convolution with kernel size of 3, stride of 1 and padding size of 1, "stride conv" denotes convolution with stride of 2, "trans conv" denotes transpose convolution, and "ACNN" denotes the ACNN-II block (Zhou et al., 2020) as described in Table .5. As described in Equation (12), one image \hat{I}_i is fed into DRDM network and a DVF $\hat{\psi}_i^{(k)}$ is predicted.

As shown in Table .5, the network structure detail for the i^{th} ACNN-II block, where "conv" denotes convolution, "ker param" denotes kernel parameters, with "dila" as dilation rate, "str" as the stride rate, and "pad" as the padding size, "norm" denotes the instance normalization, and "act" denotes the leaky ReLU activation function with 10^{-6} negative slope. The input of ACNN is a feature map with c_i and the output is the feature map with c_{i+1} processed by three convolution or dilated convolution and activation function.

Appendix B. Baseline results for image deformation

The baseline results for image deformations are illustrated in Figure A.13 using Elastic transform (a part of BigAug) (Zhang et al., 2020) and Figure A.13 using MRBS (Eppenhof and Pluim, 2019). Notably, the deformations appear unrealistic, such as the unnaturally expanded or squeezed ventricles and the distorted body shape shown in Figure A.13 and the unnatural shearing lung in Figure A.14. These unrealistic deformations can negatively impact the effectiveness of data augmentation or data synthesis, as validated by the experimental results in Section 4 and Section 5.

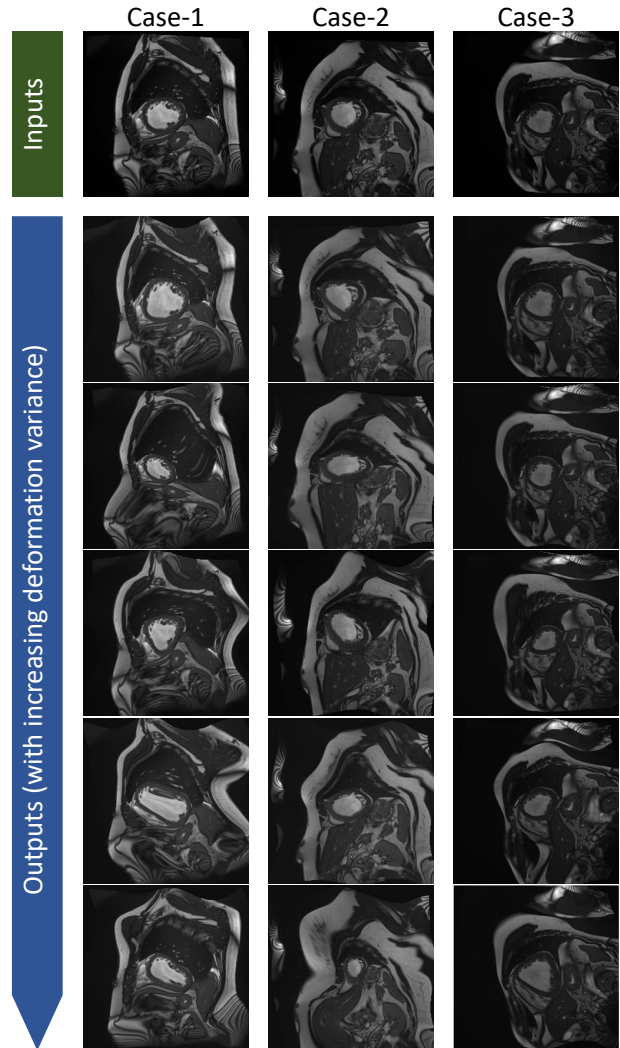


Figure A.13: The original and deformed images of three subjects by Elastic transformation as used in BigAug for 2D cardiac MRI scans.

Table .4: Network structure detail for DRDM.

func	spatial size	#chnl in/out	in	out
embed	1,1,1	1/80	t	t0
fc,act,fc	1,1,1	80/1	t0	t1
fc,act,fc	1,1,1	80/10	t0	t2
fc,act,fc	1,1,1	80/20	t0	t3
fc,act,fc	1,1,1	80/40	t0	t4
fc,act,fc	1,1,1	80/80	t0	t5
fc,act,fc	1,1,1	80/40	t0	t6
fc,act,fc	1,1,1	80/20	t0	t7
ACNN	H,W,D	$c_0/10$	$\hat{\mathbf{I}}_t+t1$	f1
ACNN	H,W,D	10/10	f1	f1
ACNN	H,W,D	10/10	f1	f1
stride conv	H/2,W/2,D/2	10/10	f1	f2
ACNN	H/2,W/2,D/2	10/20	f2+t2	f2
ACNN	H/2,W/2,D/2	20/20	f2	f2
ACNN	H/2,W/2,D/2	20/20	f2	f2
stride conv	H/4,W/4,D/4	20/20	f2	f3
ACNN	H/4,W/4,D/4	20/40	f3+t3	f3
ACNN	H/4,W/4,D/4	40/40	f3	f3
ACNN	H/4,W/4,D/4	40/40	f3	f3
stride conv	H/8,W/8,D/8	40/40	f3	f4
ACNN	H/8,W/8,D/8	40/20	f4×t4	f4
ACNN	H/8,W/8,D/8	20/20	f4	f4
ACNN	H/8,W/8,D/8	20/40	f4	f4
trans conv	H/4,W/4,D/4	40/40	f4	f5
ACNN	H/4,W/4,D/4	80/40	f5 f3+t5	f5
ACNN	H/4,W/4,D/4	40/20	f5	f5
ACNN	H/4,W/4,D/4	20/20	f5	f5
trans conv	H/2,W/2,D/2	20/20	f5	f6
ACNN	H/2,W/2,D/2	40/20	f6 f2+t6	f6
ACNN	H/2,W/2,D/2	20/10	f6	f6
ACNN	H/2,W/2,D/2	10/10	f6	f6
trans conv	H,W,D	10/10	f6	f7
ACNN	H,W,D	20/10	f7 f1+t7	f7
ACNN	H,W,D	10/10	f7	f7
ACNN	H,W,D	10/10	f7	f7
conv	H,W,D	10/3	f7	$\hat{\psi}_t^{(k)}$

Table .5: Network structure detail for the i^{th} ACNN-II block.

func	kern param dila/str/pad	#chnl in/out	in	out
conv,norm	1/1/1	c_i/c_{i+1}	fi	r
act,conv	1/1/1	c_{i+1}/c_{i+1}	r	fo
act,conv	3/1/3	c_{i+1}/c_{i+1}	fo	fo
act	-	c_{i+1}/c_{i+1}	(fo+r)	fo

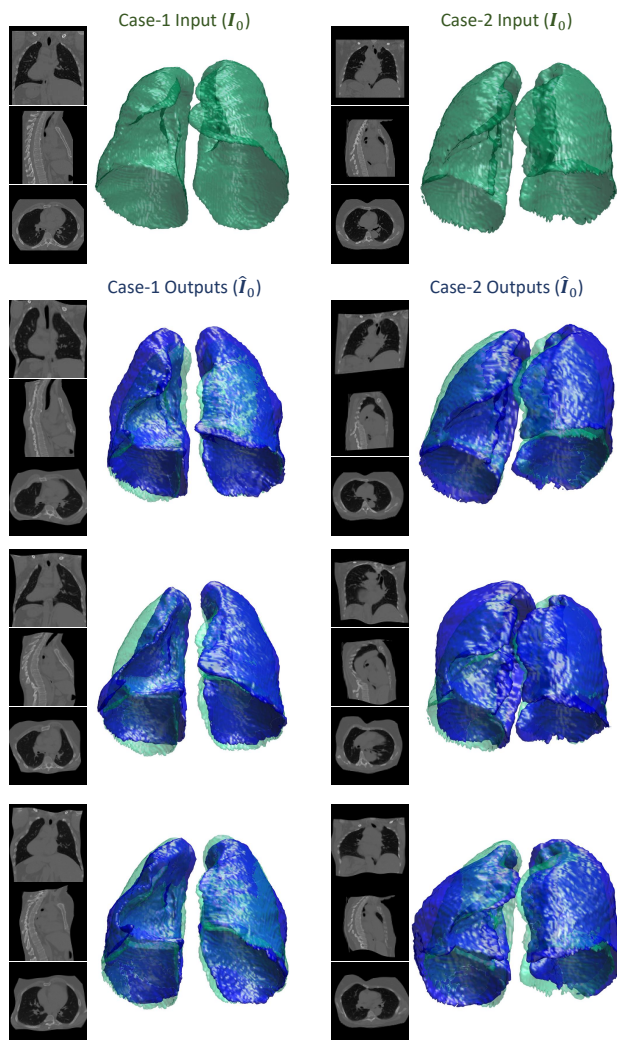


Figure A.14: The original and deformed images of two subjects by MRBS for 3D pulmonary CT scans.

References

- Aerts, H., Velazquez, E.R., Leijenaar, R., Parmar, C., Grossmann, P., Cavalho, S., Bussink, J., Monshouwer, R., Haibe-Kains, B., Rietveld, D., Hoebbers, F., Rietbergen, M.M., Leemans, C.R., Dekker, A., Quackenbush, J., Gillies, R.J., Lambin, P., 2015. Qdata from nsclc-radiomics. The cancer imaging archive doi:10.7937/K9/TCIA.2015.PF0M9REI.
- Balakrishnan, G., Zhao, A., Sabuncu, M.R., Guttag, J., Dalca, A.V., 2019. Voxelmorph: a learning framework for deformable medical image registration. *IEEE Transactions on Medical Imaging* 38, 1788–1800. doi:10.1109/TMI.2019.2897538.
- Bercea, C.I., Neumayr, M., Rueckert, D., Schnabel, J.A., 2023. Mask, stitch, and re-sample: Enhancing robustness and generalizability in anomaly detection through automatic diffusion models, in: *ICML 3rd Workshop on Interpretable Machine Learning in Healthcare (IMLH)*.
- Bernard, O., Lalande, A., Zotti, C., Cervenansky, F., Yang, X., Heng, P.A., Cetin, I., Lekadir, K., Camara, O., Gonzalez Ballester, M.A., Sanroma, G., Napel, S., Petersen, S., Tziritas, G., Grinias, E., Khened, M., Kollerathu, V.A., Krishnamurthi, G., Rohé, M.M., Pennec, X., Sermesant, M., Isensee, F., Jäger, P., Maier-Hein, K.H., Full, P.M., Wolf, I., Engelhardt, S., Baumgartner, C.F., Koch, L.M., Wolterink, J.M., Išgum, I., Jang, Y., Hong, Y., Patravali, J., Jain, S., Humbert, O., Jodoin, P.M., 2018. Deep learning techniques for automatic mri cardiac multi-structures segmentation and diagnosis: is the problem solved? *IEEE Transactions on medical imaging* 37, 2514–2525. doi:10.1109/TMI.2018.2837502.
- Bortsova, G., Dubost, F., Hogeweg, L., Katramados, I., De Bruijne, M., 2019. Semi-supervised medical image segmentation via learning consistency under transformations, in: *Medical Image Computing and Computer Assisted Intervention—MICCAI 2019: 22nd International Conference, Shenzhen, China, October 13–17, 2019, Proceedings, Part VI* 22, Springer. pp. 810–818. doi:10.1007/978-3-030-32226-7_90.
- Campello, V.M., Gkontra, P., Izquierdo, C., Martín-Isla, C., Sojoudi, A., Full, P.M., Maier-Hein, K., Zhang, Y., He, Z., Ma, J., Parreño, M., Albiol, A., Kong, F., Shadden, S.C., Corral Acero, J., Sundaresan, V., Saber, M., Elattar, M., Li, H., Menze, B., Khader, F., Haarbuerger, C., Scannell, C.M., Veta, M., Carscadden, A., Punithakumar, K., Liu, X., Tsiftaris, S.A., Huang, X., Yang, X., Li, L., Zhuang, X., Viladés, D., Descalzo, M.L., Guala, A., La Mura, L., Friedrich, M.G., Garg, R., Lebel, J., Henriques, F., Karakas, M., Çavuş, E., Petersen, S.E., Escalera, S., Seguí, S., Rodríguez-Palomares, J.F., Lekadir, K., 2021. Multi-centre, multi-vendor and multi-disease cardiac segmentation: the m&ms challenge. *IEEE Transactions on Medical Imaging* 40, 3543–3554. doi:10.1109/TMI.2021.3090082.
- Christensen, G.E., Rabbitt, R.D., Miller, M.I., 1996. Deformable templates using large deformation kinematics. *IEEE transactions on image processing* 5, 1435–1447. doi:10.1109/83.536892.
- Dang, V.N., Galati, F., Cortese, R., Di Giacomo, G., Marconetto, V., Mathur, P., Lekadir, K., Lorenzi, M., Prados, F., Zuluaga, M.A., 2022. Vessel-captcha: an efficient learning framework for vessel annotation and segmentation. *Medical Image Analysis* 75, 102263. doi:10.1016/j.media.2021.102263.
- Davis, M.H., Khotanzad, A., Flamig, D.P., Harms, S.E., 1997. A physics-based coordinate transformation for 3-d image matching. *IEEE Transactions on medical imaging* 16, 317–328. doi:10.1109/42.585766.
- Du, Y., Jiang, Y., Tan, S., Wu, X., Dou, Q., Li, Z., Li, G., Wan, X., 2023. Arsdm: colonoscopy images synthesis with adaptive refinement semantic diffusion models, in: *International conference on medical image computing and computer-assisted intervention*, Springer. pp. 339–349. doi:10.1007/978-3-031-43895-0_32.
- Eppenhof, K.A., Pluim, J.P., 2019. Pulmonary ct registration through supervised learning with convolutional neural networks. *IEEE Transactions on medical imaging* 38, 1097–1105. doi:10.1109/TMI.2018.2878316.

- Gao, F., He, Y., Li, S., Hao, A., Cao, D., 2023. Diffusing coupling high-frequency-purifying structure feature extraction for brain multimodal registration, in: 2023 IEEE International Conference on Bioinformatics and Biomedicine (BIBM), IEEE. pp. 508–515. doi:10.1109/BIBM58861.2023.10385725.
- Gong, S., Chen, C., Gong, Y., Chan, N.Y., Ma, W., Mak, C.H.K., Abrigo, J., Dou, Q., 2023. Diffusion model based semi-supervised learning on brain hemorrhage images for efficient midline shift quantification, in: International Conference on Information Processing in Medical Imaging, Springer. pp. 69–81. doi:10.1007/978-3-031-34048-2_6.
- Gonzales, R.A., Zhang, Q., Papież, B.W., Werys, K., Lukaschuk, E., Popescu, I.A., Burrage, M.K., Shanmuganathan, M., Ferreira, V.M., Piechnik, S.K., 2021. Moconet: robust motion correction of cardiovascular magnetic resonance t1 mapping using convolutional neural networks. *Frontiers in Cardiovascular Medicine* 8, 768245. doi:10.3389/fcvm.2021.768245.
- Goodfellow, I., Pouget-Abadie, J., Mirza, M., Xu, B., Warde-Farley, D., Ozair, S., Courville, A., Bengio, Y., 2020. Generative adversarial networks. *Communications of the ACM* 63, 139–144. doi:10.1145/3422622.
- Graf, R., Schmitt, J., Schlaeger, S., Möller, H.K., Sideri-Lampretsa, V., Sekuboyina, A., Krieg, S.M., Wiestler, B., Menze, B., Rueckert, D., et al., 2023. Denoising diffusion-based mri to ct image translation enables automated spinal segmentation. *European Radiology Experimental* 7, 70. doi:10.1186/s41747-023-00385-2.
- Gu, A., Dao, T., 2023. Mamba: Linear-time sequence modeling with selective state spaces. *arXiv preprint arXiv:2312.00752* doi:10.48550/arXiv.2312.00752.
- Hering, A., Hansen, L., Mok, T.C., Chung, A.C., Siebert, H., Häger, S., Lange, A., Kuckertz, S., Heldmann, S., Shao, W., Vesal, S., Rusu, M., Sonn, G., Estienne, T., Vakalopoulou, M., Han, L., Huang, Y., Yap, P.T., Balbastre, Y., Joutard, S., Modat, M., Lifshitz, G., Raviv, D., Lv, J., Li, Q., Jaouen, V., Visvikis, D., Fourcade, C., Rubeaux, M., Pan, W., Xu, Z., Jian, B., Benetti, F.D., Wodzinski, M., Gunnarsson, N., Sjölund, J., Grzech, D., Qiu, H., Li, Z., Duan, J., Großbröhmer, C., Reinertsen, I., Xiao, Y., Landman, B., Huo, Y., Murphy, K., Lessmann, N., Ginneken, B.v., Dalca, A.V., Heinrich, M.P., 2022. Learn2reg: comprehensive multi-task medical image registration challenge, dataset and evaluation in the era of deep learning. *IEEE Transactions on Medical Imaging* 42, 697–712. doi:10.1109/TMI.2022.3213983.
- Ho, J., Jain, A., Abbeel, P., 2020. Denoising diffusion probabilistic models. *Advances in neural information processing systems* 33, 6840–6851. doi:10.5555/3495724.3496298.
- Islam, M.A., Jia, S., Bruce, N.D., 2019. How much position information do convolutional neural networks encode?, in: International Conference on Learning Representations.
- Jaderberg, M., Simonyan, K., Zisserman, A., kavukcuoglu, k., 2015. Spatial transformer networks. *Advances in Neural Information Processing Systems* 28, 2017–2025. doi:10.5555/2969442.2969465.
- Jayasumana, S., Ramalingam, S., Veit, A., Glasner, D., Chakrabarti, A., Kumar, S., 2024. Rethinking fid: Towards a better evaluation metric for image generation, in: Proceedings of the IEEE/CVF Conference on Computer Vision and Pattern Recognition, pp. 9307–9315.
- Ju, Z., Zhou, W., 2024. Vm-ddpm: Vision mamba diffusion for medical image synthesis. *arXiv preprint arXiv:2405.05667* doi:10.48550/arXiv.2405.05667.
- Kalpathy-Cramer, J., Napel, S., Goldgof, D., Zhao, B., 2015. Qin multi-site collection of lung ct data with nodule segmentations. *Cancer Imaging Arch* 10, K9.
- Kazerouni, A., Aghdam, E.K., Heidari, M., Azad, R., Fayyaz, M., Hacihaliloglu, I., Merhof, D., 2023. Diffusion models in medical imaging: A comprehensive survey. *Medical Image Analysis* 88, 102846. doi:10.1016/j.media.2023.102846.

- Kim, B., Han, I., Ye, J.C., 2022. Diffusemorph: Un-supervised deformable image registration using diffusion model, in: European conference on computer vision, Springer. pp. 347–364. doi:10.1007/978-3-031-19821-2_20.
- Kim, B., Ye, J.C., 2022. Diffusion deformable model for 4d temporal medical image generation, in: International Conference on Medical Image Computing and Computer-Assisted Intervention, Springer. pp. 539–548. doi:10.1007/978-3-031-16431-6_51.
- Kingma, D.P., Welling, M., 2013. Auto-encoding variational bayes. arXiv preprint arXiv:1312.6114 doi:10.48550/arXiv.1312.6114.
- Lee, S., Wolberg, G., Shin, S.Y., 1997. Scattered data interpolation with multilevel b-splines. IEEE transactions on visualization and computer graphics 3, 228–244. doi:10.1109/2945.620490.
- Li, J., Cao, H., Wang, J., Liu, F., Dou, Q., Chen, G., Heng, P.A., 2023. Fast non-markovian diffusion model for weakly supervised anomaly detection in brain mr images, in: International Conference on Medical Image Computing and Computer-Assisted Intervention, Springer. pp. 579–589. doi:10.1007/978-3-031-43904-9_56.
- Liang, Z., Anthony, H., Wagner, F., Kamnitsas, K., 2023. Modality cycles with masked conditional diffusion for unsupervised anomaly segmentation in mri, in: International Conference on Medical Image Computing and Computer-Assisted Intervention, Springer. pp. 168–181. doi:10.1007/978-3-031-47425-5_16.
- Martín-Isla, C., Campello, V.M., Izquierdo, C., Kushibar, K., Sendra-Balcells, C., Gkontra, P., Sojoudi, A., Fulton, M.J., Arega, T.W., Punithakumar, K., Li, L., Sun, X., Khalil, Y.A., Liu, D., Jabbar, S., Queirós, S., Galati, F., Mazher, M., Gao, Z., Beetz, M., Tautz, L., Galazis, C., Varela, M., Hüllebrand, M., Grau, V., Zhuang, X., Puig, D., Zuluaga, M.A., Mohy-ud Din, H., Metaxas, D., Breeuwer, M., Geest, R.J.v.d., Noga, M., Bricq, S., Rentschler, M.E., Guala, A., Petersen, S.E., Escalera, S., Palomares, J.F.R., Lekadir, K., 2023. Deep learning segmentation of the right ventricle in cardiac mri: The m&ms challenge. IEEE Journal of Biomedical and Health Informatics 27, 3302–3313. doi:10.1109/JBHI.2023.3267857.
- Mo, Y., Liu, F., Yang, G., Wang, S., Zheng, J., Wu, F., Papież, B.W., McIlwraith, D., He, T., Guo, Y., 2024. Labelling with dynamics: A data-efficient learning paradigm for medical image segmentation. Medical Image Analysis , 103196doi:10.1016/j.media.2024.103196.
- Pinaya, W.H., Tudosi, P.D., Dafflon, J., Da Costa, P.F., Fernandez, V., Nachev, P., Ourselin, S., Cardoso, M.J., 2022. Brain imaging generation with latent diffusion models, in: MICCAI Workshop on Deep Generative Models, Springer. pp. 117–126. doi:10.1007/978-3-031-18576-2_12.
- Qiao, T., Zhang, J., Xu, D., Tao, D., 2019. Mirrorgan: Learning text-to-image generation by redescription, in: Proceedings of the IEEE/CVF conference on computer vision and pattern recognition, pp. 1505–1514. doi:10.1109/CVPR.2019.00160.
- Qin, Y., Li, X., 2023. Fsdiffreg: Feature-wise and score-wise diffusion-guided unsupervised deformable image registration for cardiac images, in: International Conference on Medical Image Computing and Computer-Assisted Intervention, Springer. pp. 655–665. doi:10.1007/978-3-031-43999-5_62.
- Radau, P., Lu, Y., Connelly, K., Paul, G., Dick, A.J., Wright, G.A., 2009. Evaluation framework for algorithms segmenting short axis cardiac mri. The MIDAS Journal doi:10.54294/g80ruo.
- Rohé, M.M., Datar, M., Heimann, T., Sermesant, M., Pennec, X., 2017. Svf-net: learning deformable image registration using shape matching, in: Medical Image Computing and Computer Assisted Intervention-MICCAI 2017: 20th International Conference, Quebec City, QC, Canada, September 11-13, 2017, Proceedings, Part I 20, Springer. pp. 266–274. doi:10.1007/978-3-319-66182-7_31.
- Rombach, R., Blattmann, A., Lorenz, D., Esser, P., Ommer, B., 2022. High-resolution image synthesis with latent diffusion models, in: Proceedings of the

- IEEE/CVF conference on computer vision and pattern recognition, pp. 10684–10695. doi:10.1109/CVPR52688.2022.01042.
- Ronneberger, O., Fischer, P., Brox, T., 2015. U-net: Convolutional networks for biomedical image segmentation, in: International Conference on Medical Image Computing and Computer-Assisted Intervention, Springer. pp. 234–241. doi:10.1007/978-3-319-24574-4_28.
- Sohl-Dickstein, J., Weiss, E., Maheswaranathan, N., Ganguli, S., 2015. Deep unsupervised learning using nonequilibrium thermodynamics, in: International conference on machine learning, PMLR. pp. 2256–2265. doi:10.5555/3045118.3045358.
- Sokooti, H., De Vos, B., Berendsen, F., Lelieveldt, B.P., Išgum, I., Staring, M., 2017. Nonrigid image registration using multi-scale 3d convolutional neural networks, in: Medical Image Computing and Computer Assisted Intervention- MICCAI 2017: 20th International Conference, Quebec City, QC, Canada, September 11-13, 2017, Proceedings, Part I 20, Springer. pp. 232–239. doi:10.1007/978-3-319-66182-7_27.
- Song, J., Meng, C., Ermon, S., 2020. Denoising diffusion implicit models, in: International Conference on Learning Representations.
- Starck, S., Sideri-Lampretsa, V., Kainz, B., Menten, M., Mueller, T., Rueckert, D., 2024. Diff-def: Diffusion-generated deformation fields for conditional atlases. arXiv preprint arXiv:2403.16776 doi:10.48550/arXiv.2403.16776.
- Tobon-Gomez, C., Geers, A.J., Peters, J., Weese, J., Pinto, K., Karim, R., Ammar, M., Daoudi, A., Margeta, J., Sandoval, Z., Stender, B., Zheng, Y., Zuluaga, M.A., Betancur, J., Ayache, N., Chikh, M.A., Dillenseger, J.L., Kelm, B.M., Mahmoudi, S., Ourselin, S., Schläfer, A., Schaeffter, T., Razavi, R., Rhode, K.S., 2015. Benchmark for algorithms segmenting the left atrium from 3d ct and mri datasets. *IEEE transactions on medical imaging* 34, 1460–1473. doi:10.1109/TMI.2015.2398818.
- Uzunova, H., Wilms, M., Handels, H., Ehrhardt, J., 2017. Training cnns for image registration from few samples with model-based data augmentation, in: Medical Image Computing and Computer Assisted Intervention- MICCAI 2017: 20th International Conference, Quebec City, QC, Canada, September 11-13, 2017, Proceedings, Part I 20, Springer. pp. 223–231. doi:10.1007/978-3-319-66182-7_26.
- Vercauteren, T., Pennec, X., Perchant, A., Ayache, N., 2009. Diffeomorphic demons: Efficient non-parametric image registration. *NeuroImage* 45, S61–S72. doi:10.1016/j.neuroimage.2008.10.040.
- Wang, Z., Li, T., Zheng, J.Q., Huang, B., 2022a. When cnn meet with vit: Towards semi-supervised learning for multi-class medical image semantic segmentation, in: European Conference on Computer Vision, Springer. pp. 424–441. doi:10.1007/978-3-031-25082-8_28.
- Wang, Z., Zheng, J.Q., Voiculescu, I., 2022b. An uncertainty-aware transformer for mri cardiac semantic segmentation via mean teachers, in: Annual Conference on Medical Image Understanding and Analysis, Springer. pp. 494–507. doi:10.1007/978-3-031-12053-4_37.
- Wilms, M., Handels, H., Ehrhardt, J., 2017. Multi-resolution multi-object statistical shape models based on the locality assumption. *Medical image analysis* 38, 17–29. doi:10.1016/j.media.2017.02.003.
- Wolleb, J., Bieder, F., Sandkühler, R., Cattin, P.C., 2022. Diffusion models for medical anomaly detection, in: International Conference on Medical image computing and computer-assisted intervention, Springer. pp. 35–45. doi:10.1007/978-3-031-16452-1_4.
- Zhan, F., Yu, Y., Wu, R., Zhang, J., Lu, S., Liu, L., Kortylewski, A., Theobalt, C., Xing, E., 2023. Multimodal image synthesis and editing: A survey and taxonomy. *IEEE Transactions on Pattern Analysis and Machine Intelligence* doi:10.1109/TPAMI.2023.3305243.
- Zhang, L., Wang, X., Yang, D., Sanford, T., Harmon, S., Turkbey, B., Wood, B.J., Roth, H., Myronenko, A., Xu, D., Xu, Z., 2020. Generalizing deep learning for medical image segmentation to unseen domains via deep

- stacked transformation. *IEEE Transactions on Medical Imaging* 39, 2531–2540. doi:10.1109/TMI.2020.2973595.
- Zhao, A., Balakrishnan, G., Durand, F., Guttag, J.V., Dalca, A.V., 2019. Data augmentation using learned transformations for one-shot medical image segmentation, in: *Proceedings of the IEEE/CVF conference on computer vision and pattern recognition*, pp. 8543–8553. doi:10.1109/CVPR.2019.00874.
- Zheng, J.Q., Lim, N.H., Papież, B.W., 2023. Accurate volume alignment of arbitrarily oriented tibiae based on a mutual attention network for osteoarthritis analysis. *Computerized Medical Imaging and Graphics* 106, 102204. doi:10.1016/j.compmedimag.2023.102204.
- Zheng, J.Q., Wang, Z., Huang, B., Lim, N.H., Papież, B.W., 2024. Residual aligner-based network (ran): Motion-separable structure for coarse-to-fine deformable image registration. *Medical Image Analysis*, 103038doi:10.1016/j.media.2023.103038.
- Zheng, J.Q., Wang, Z., Huang, B., Vincent, T., Lim, N.H., Papież, B.W., 2022. Recursive deformable image registration network with mutual attention, in: *Annual Conference on Medical Image Understanding and Analysis*, Springer. pp. 75–86. doi:10.1007/978-3-031-12053-4_6.
- Zhou, X.Y., Zheng, J.Q., Li, P., Yang, G.Z., 2020. ACNN: a full resolution dcnn for medical image segmentation, in: *2020 IEEE International Conference on Robotics and Automation (ICRA)*, IEEE. pp. 8455–8461. doi:10.1109/ICRA40945.2020.9197328.